Petrophysics of Chicxulub Impact Crater's Peak Ring

E. Le Ber, D. Loggia, N. Denchik, J. Lofi, D. A. Kring, P. Sardini, M. Siitari-Kauppi, P. Pezard, G. Olivier

JGR Solid Earth

RESEARCH ARTICLE
10.1029/2021JB023801

Petrophysics of Chicxulub Impact Crater's Peak Ring

E. Le Ber[1], D. Loggia[1], N. Denchik[1], J. Lofi[1], D. A. Kring[2], P. Sardini[3], M. Siitari-Kauppi[4], P. Pezard[1], G. Olivier[3], and IODP-ICDP Expedition 364 Science Party[5]

[1]Géosciences Montpellier, Université de Montpellier (UMR5243), CNRS, Montpellier, France, [2]Lunar and Planetary Institute, Universities Space Research Association, Houston, TX, USA, [3]Institut de Chimie des Milieux et des Matériaux de Poitiers (IC2MP), Université de Poitiers, Poitiers, France, [4]Department of Chemistry, University of Helsinki, Helsinki, Finland, [5]See Appendix A

Key Points:

- Independant petrophysical measurements are used to caracterize the nature of the porosity in Chicxulub impact crater's peak ring
- Shocked granites behave more like a cemented clastic rock than a fractured crystalline rock
- Matrix permeabilities of peak-ring lithologies bring new insight on fluid flow in postimpact hydrothermal systems

Correspondence to:
E. Le Ber,
erwan.le-ber@umontpellier.fr

Citation:
Le Ber, E., Loggia, D., Denchik, N., Lofi, J., Kring, D. A., Sardini, P., et al. (2022). Petrophysics of Chicxulub impact crater's peak ring. *Journal of Geophysical Research: Solid Earth*, *127*, e2021JB023801. https://doi.org/10.1029/2021JB023801

Received 10 DEC 2021
Accepted 13 APR 2022

Author Contributions:
Conceptualization: E. Le Ber, D. Loggia, J. Lofi
Data curation: E. Le Ber, D. Loggia, P. Pezard
Formal analysis: E. Le Ber, D. Loggia, N. Denchik, P. Sardini, M. Siitari-Kauppi, P. Pezard, G. Olivier
Investigation: D. Loggia
Methodology: D. Loggia, N. Denchik, P. Sardini
Project Administration: J. Lofi
Resources: J. Lofi, P. Sardini, M. Siitari-Kauppi
Software: D. Loggia
Supervision: D. Loggia, J. Lofi, P. Sardini
Validation: E. Le Ber, N. Denchik, J. Lofi, D. A. Kring, M. Siitari-Kauppi, P. Pezard
Visualization: E. Le Ber

Abstract

A new set of physical property measurements was undertaken on 29 peak-ring samples from the IODP-ICDP Expedition 364. Among the studied lithologies, the dominant one recovered in the peak ring consists of shocked granitoid rocks (19 samples). Porosity measurements with two independent methods (triple weight and ^{14}C-PMMA porosity mapping) concur and bring new observations on the intensity and distribution of fracturing and porosity in these shocked target rocks. Characterization of the porous network is taken a step further with two other independent methods (electrical and permeability measurements). Electrical properties such as the cementation exponent ($1.59 < m < 1.87$) and the formation factor ($21 < F < 103$) do not compare with other granites from the published literature; they point at a type of porosity closer to clastic sedimentary rocks than to crystalline rocks. Permeabilities of the granitoid rocks range from 0.1 to 7.1 mD under an effective pressure of ∼10 MPa. Unlike other fresh to deformed and altered granitoid rocks from the literature compared in this study, this permeability appears to be relatively insensitive to increasing stress (up to ∼40 MPa), with implications for the nature of the porous network, again, behaving more like cemented clastic rocks than fractured crystalline rocks. Other analyzed lithologies include suevite and impact melt rocks. Relatively low permeability (10^{-3} mD) measured in melt-rich facies suggest that, at the matrix scale, these lithologies cutting through more permeable peak-ring granitoid rocks may have been a barrier to fluid flow, with implications for hydrothermal systems.

Plain Language Summary

Sixty-six million years ago, a 10–15 km sized meteorite ended its trajectory on Earth. The resulting crater, Chicxulub, is still preserved to this day in Mexico. The impact had dramatic consequences on Earth's organisms. Drilled core samples from its peak ring help to better understand what are the physical mechanisms involved in such large impact events, on Earth and other planets. This study looks at how the rocks shocked during the impact have been affected, they consist principally of granites. Intact granites are crystalline rocks known to have low porosity (<2%), typically resulting from microscopic cracks. Granites recovered from the crater have higher porosities (∼10%) and are so densely cracked that they behave more like a sandstone than cracked crystalline rocks. This observation results from physical measurements, presented in this paper, that also suggested that fluid can flow relatively easily in these granites, with implications for hydrothermal systems and life in the aftermath of the impact.

1. Introduction

Physical properties of impact structures are critical in understanding how the target rocks are affected during and after an impact event. They provide observational constraints that can calibrate numerical models used to simulate cratering and postimpact processes. Existing models suggest that large impact events will heat subsurface water in porous permeable crater interiors and generate hydrothermal systems (Abramov & Kring, 2004, 2007; Rathbun & Squyres, 2002). Hydrothermal alteration is observed in impact sites (Kring & Boynton, 1992; McCarville & Crossey, 1996; Morgan et al., 2016; Naumov, 1996; Osinski et al., 2001) and such systems may have provided niches for microbial ecosystems early in Earth history (Cockell, 2006; Kring, 2000; Kring & Bach, 2021; Kring et al., 2020, 2021). A key parameter in existing models is permeability, which can strongly affect the duration of impact-generated hydrothermal activity. Large, well preserved, impact structures are uncommon on Earth's surface, therefore opportunities to test those models with direct measurements of permeability and other physical parameters of crater lithologies are rare.

Writing – original draft: E. Le Ber, D. Loggia, D. A. Kring, P. Sardini

The best preserved impact basin on Earth is the Chicxulub impact crater, which sits beneath the northern coast of Yucatán. Although the crater is not accessible at the surface, it is preserved from erosion under Cenozoic sediments. The Chicxulub crater is an ideal candidate to explore the physical properties of an impact structure. Its peak ring was successfully sampled offshore in 2016 by the IODP-ICDP Expedition 364 (Morgan et al., 2017), from 617.33 to 1334.68 m below the seafloor (mbsf). The Chicxulub impact crater target rocks from that core consist mostly of granitoid rocks that were shocked during the impact, suevites, and impact melt rocks. This study integrates new petrophysical measurements of those peak-ring rocks in order to help understand their transport properties, i.e., the permeability and electrical conductivity, in relation with the porosity (including porosity mapping autoradiography).

The dominant lithology from the recovered section consists of granitoid rocks that are pervasively shocked and structurally altered (Rae et al., 2019a, 2019b; Riller et al., 2018). Compared to intact granites, the main petrophysical change observed in those shocked granitoid rocks is an increase in porosity, associated with a decrease in bulk density (Christeson et al., 2018; Morgan et al., 2016, 2017). In terms of crater size and peak-ring lithologies, there are few known equivalents on Earth, and none with available peak-ring data to compare it with. The petrophysical data collected on Chicxulub's granitoid rocks presented in this study are compared with other existing intact and altered granite data from the literature, representing a variety of geological settings (e.g., water reservoirs, tectonically active settings, hydrothermal systems, nuclear waste site storage investigations).

2. Geological Context

2.1. Hole M0077A

The Chicxulub impact crater is ∼180 km in diameter and features a peak ring, which is an inner ring of uplifted rock ∼80-km diameter that is typical of large impact structures. The 2016 IODP-ICDP Expedition 364 drilled off the coast of Yucatán, in part to recover core of the peak ring that could be used to evaluate the physical processes involved in the formation of large impact craters and peak rings (Gulick et al., 2016). Hole M0077A reached a total depth of 1334.68 mbsf. Core lithologies recovered include postimpact carbonate sediments (Unit 1, 505.7–617.33 mbsf) deposited on the top of the peak ring, consisting of impact melt-bearing polymict breccias called suevites (Unit 2, 617.33–721.62 mbsf), impact melt rocks (Unit 3, 721.62–747.02 mbsf), and shocked target rocks with intervals of suevite and impact melt rocks (Unit 4, 747.02–1334.68 mbsf; Morgan et al., 2017).

Among the set of IODP shipboard data, physical properties collected (on cores and downhole) from the peak ring were crucial to understand the physical processes that occurred during and after the impact (Morgan et al., 2016; Riller et al., 2018). The formation of the peak ring results from the outward collapse of the central uplift of the target rocks (basement) during crater formation. Granitoid rocks recovered during the expedition moved >20 km in <10 min at the time of the impact (Morgan et al., 2016). Petrophysical measurements, computed tomography (CT-scans), and core descriptions indicate the rocks of the peak ring, dominated by shocked granitoid rocks, have higher porosity and lower density than intact granites (Christeson et al., 2018; Morgan et al., 2017; Rae et al., 2019a). These changes in physical properties result mainly from shock-induced microfracturing during the impact event (Rae et al., 2019a, 2019b; Riller et al., 2018). Alteration of the rocks also suggests fluid circulation in the peak ring in the aftermath of the impact, associated with an hydrothermal system that may have lasted >2 million years (Kring et al., 2020, 2021; Simpson et al., 2020; Timms et al., 2020).

2.2. Sample Description

In addition to expedition shipboard data already published (Christeson et al., 2018; Morgan et al., 2017), this study provides new laboratory petrophysical data relevant to the nature of the porosity in the peak ring. In order to represent the diversity of recovered lithologies and alteration, a selection of 29 samples (6 suevites, 3 impact melt rocks, 1 mixture of granite and cataclasite, and 19 granitoid rocks—Figure 1) was measured for density, porosity, permeability, electrical conductivity (allowing the calculation of the formation factor and surface conductivity), and dry and wet *P* wave velocity. Of these samples, two granitoid rocks were also analyzed with autoradiography ^{14}C-PMMA method.

The samples (mini-cores) selected for this study consist of 2-cm diameter plugs, ∼3-cm long extracted from the working halves of the cores; these same samples were originally used to measure discrete *P* wave (DPW)

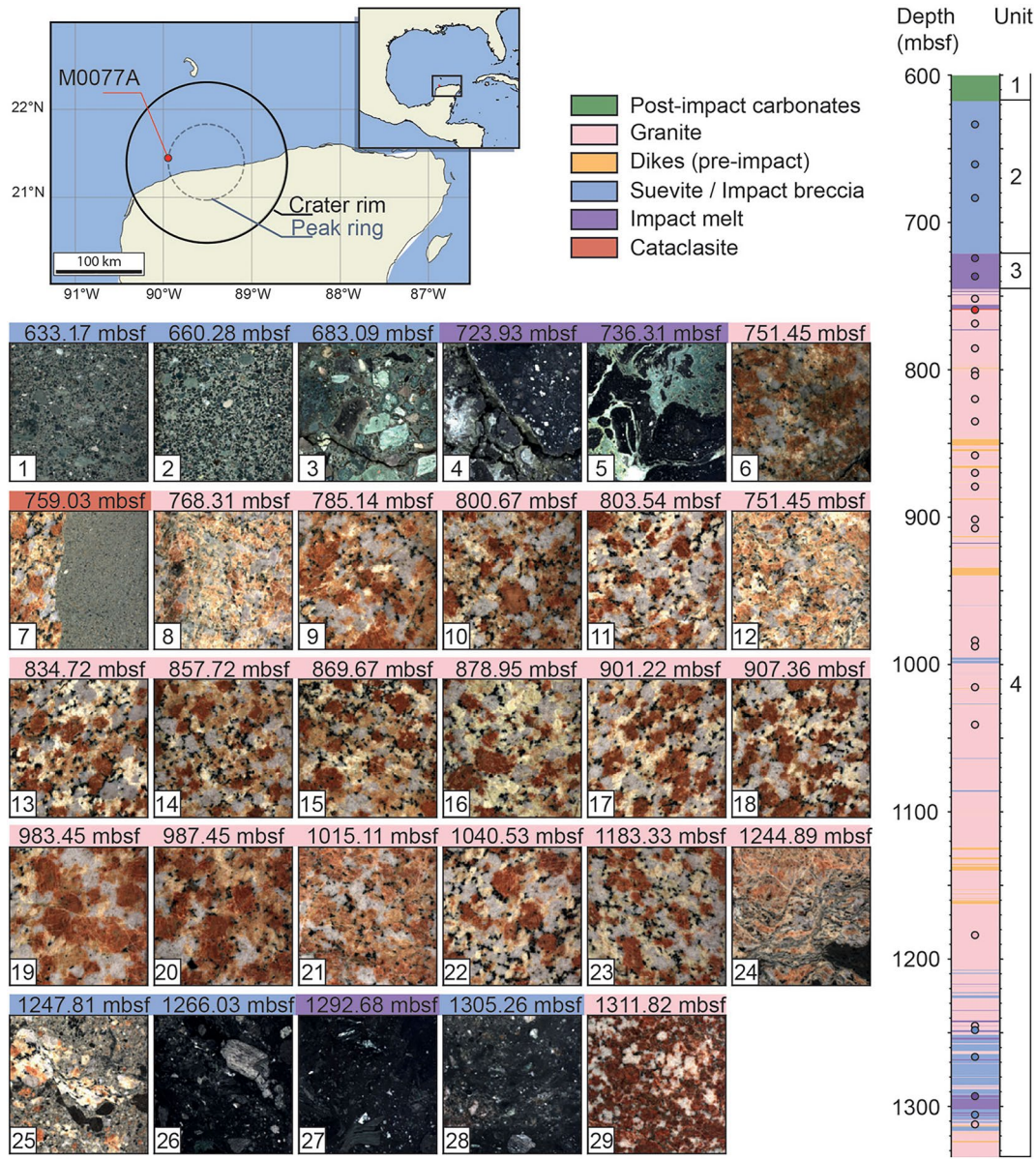

Figure 1. M0077A. Location, units, lithostratigraphy, and selected samples overview. Image patches are ~7.2 × 7.2 cm and were extracted from the linescans (https://doi.pangaea.de/10.1594/PANGAEA.881718) of the core archive halves, to the corresponding depth of the samples that were extracted from the working halves.

velocities at the time of the expedition. An illustrated summary of those sample lithologies is shown in Figure 1. Each sample is matched with a representative image patch (squares with an edge of ~7.2 cm) extracted at the same depth on the archive half digital scan of the core.

2.2.1. Suevites

Suevites are polymict breccias that contain fragments of solidified melt produced by impact events (Stöffler & Grieve, 2007). Suevite occurs at several intervals in the core. The top of the peak ring in Hole M0077A is covered with ~104 m of suevite with variable clast size and lithology (Kaskes et al., 2021). Clast dimensions range from submillimeter to several centimeters; in general, clast size increases with depth (Gulick et al., 2019; Morgan et al., 2017). This portion of suevite is Unit 2 in the logged upper peak-ring sequence. Samples 1, 2, and 3 in this study are clast-supported suevites from this unit. Clasts consist principally of limestones and solidified melt that are cemented by a micritic carbonate matrix.

Sample 25 occurs in Unit 4 toward the bottom of the hole, in a complex ~2-m-thick interval, where mixed melt and suevite cut through granitic target rocks (or a block derived from target rocks). This sample consists principally of a cm-scale partially melted granite fragment in contact with a dense fine-grained suevite (sub-mm clasts). Samples 26 and 28 were collected from suevite intervals that are mingled with impact melt rocks. Suevite from Unit 4 is not sorted like in Unit 2 and does not include any sedimentary clasts (Morgan et al., 2017). Samples 26 and 28 are matrix-supported suevites that include melt, granitoid rocks, and mafic sub-cm clasts. All suevite samples from Unit 4 belong to the lower impact melt rock-bearing unit described by de Graaff et al. (2021).

2.2.2. Impact Melt Rocks

Solidified impact melt rocks in Unit 3, or the upper impact melt rock unit from de Graaff et al. (2021), are a mixture of dark green and black melt rock supporting sub-cm angular target rocks, melt clasts, and a carbonate signature (de Graaff et al., 2021; Schulte et al., 2021). This study includes two samples (numbers 4 and 5) of that unit. Solidified impact melt rocks are also found in Unit 4, or the lower impact melt rock-bearing unit from de Graaff et al. (2021), it consists of a brecciated impact melt rock that is not associated with carbonate dilution. Following peak-ring lithology classification from Morgan et al. (2017), this study includes a single impact melt rock sample from Unit 4, near the bottom of the hole (number 27). However, suevite samples 25, 26, and 28 from Unit 4 are also part of de Graff et al. (2021) lower impact melt rock-bearing unit. The upper impact melt rock unit and the lower impact melt rock-bearing unit both initiated from the same initial impact melt material but their different compositions and facies reflect different emplacement history, as discussed by de Graaff et al. (2021).

2.2.3. Cataclasite

Cataclasite zones have been described in the granitoid target rocks at the microscopic and macroscopic scale (McCall et al., 2021; Rae et al., 2019a; Riller et al., 2018). Sample 7 was extracted from near the top of Unit 4 where impact melt rock is juxtaposed with granitoid rocks. Along the contact between those two lithologies is a 5-cm wide zone of cataclasite. The sample includes a sharp contact between cataclasite (two-thirds of the sample) and granitoid rock (one-third of the sample).

2.2.4. Granitoid Rocks

Granitoid rocks are the main lithologies in the recovered peak-ring cores. The texture of the target rock is generally coarse, with pink to reddish alkali-feldspar, white to pale yellow plagioclase, gray to white quartz, and dark minerals (principally biotite). The original rock underwent pervasive fracturing during the impact, followed by further deformation such as cataclasis, shear faulting (Riller et al., 2018), and impact-induced crack porosity (Rae et al., 2019a) during formation of the peak ring. Sample locations within the granitoid rocks were selected to cover both strongly altered intervals (e.g., crenulated foliation in samples 8 and 12, hydrothermalization in sample 29), as well as facies in shocked intervals that seem to have kept a more pristine texture.

3. Data and Method

3.1. Density and Porosity

Standard shipboard measurements of Moisture And Density (MAD, using a pycnometer) and DPW were acquired as part of Expedition 364 (Morgan et al., 2017). Those discrete measurements were made during the Onshore Science Party (OSP) on ~6 cm^3, 2-cm diameter plugs, extracted every ~1.5 m down the length of the core. MAD and DPW analyses were made on samples up to 10 cm apart, but always within the same lithology. This study reuses the DPW samples from the expedition to perform the measurements described in this method section, and they are compared to the shipboard MAD data set. Porosity was measured at the University of Montpellier on the mini-cores by the triple weight method (mass of dry m_{dry} (80 °C oven), saturated m_{sat} (1 g/L NaCl), and immersed samples m_{imm}) with a balance providing an accuracy of 10^{-2} g. The porosity is given by

$$\phi = \frac{m_{sat} - m_{dry}}{m_{sat} - m_{imm}}$$

This technique also provides the grain and bulk density of the sample

$$\rho_{grain} = \frac{m_{dry} \times \rho_{fluid}}{m_{dry} - m_{imm}} \; and \; \rho_{bulk} = \frac{m_{sat} \times \rho_{fluid}}{m_{sat} - m_{imm}}$$

where $\rho_{fluid} = 1$ g/cm^3.

The triple weight method offers an excellent control on water saturation for m_{sat}. Dry samples are placed into a vacuum, then satrated with a degassed fluid, ensuring all connected pore space is filled with fluid. This might not always be the case with MAD shipboard measurements, where a sample may lose some of its water content between the expedition and the measurement; and also between sampling and m_{sat} measurement.

3.2. Electrical Properties

A series of electrical conductivity measurements were carried out at the University of Montpellier on the mini-cores in order to determine the electrical properties and the geometry of the pore space (i.e., formation factor F and surface conductivity C_s). The samples were first dried (vacuum setting during 48 hr), then saturated with five different saturating fluid conductivities (using NaCl, C_w ranging from 0.1 to 5 S/m). For each salinity, measurements of the saturated rock conductivity C_o were made at room pressure and temperature. The electrical resistance R (in Ohm) of the mini-cores was measured using a solartron SI 1260 impedance meter at a frequency of 1,000 Hz, and C_o was then calculated with the equation

$$C_o = \frac{L}{R \times S}$$

where L and S are the length and the section of the mini-core. The formation factor and the surface conductivity were then obtained with the Waxman and Smits (1968) equation, which takes into account the electrolytic conductivity into the pore space (C_w/F) and the excess conductivity (C_s) due to surface conduction

$$C_o = \frac{C_w}{F} + C_s$$

F is related to the porosity (ϕ) and the microgeometry of the pore space. Knowing the porosity and the formation factor, it is possible to use Archie's law (Archie, 1942)

$$F = \phi^{-m}$$

and calculate the cementation exponent (m). m gives an indication on how well pores are connected. Using F and ϕ also allows the determination of electrical tortuosity (τ^2; Walsh & Brace, 1984)

$$\tau^2 = F \times \phi$$

giving information about the complexity of the path electrical currents (carried by the fluid) take to travel through the rock porosity. The other variable deduced from Waxman and Smits equation is the surface conductivity C_s. It increases with the presence of altered minerals, typically occurring at the surface of the grains.

3.3. Permeability

The gas permeability was measured at the University of Montpellier on oven dried mini-core samples under steady state conditions using the standard steady state method and Darcy's law as described in Tanikawa and Shimamoto (2009). Measurements were performed at different isotropic confined pressures ranging from ~5 to ~40 MPa, applied on the samples and a coreholder. All measured samples have at least two measurement points, at 10 and 40 MPa. Argon was injected at a constant pressure applied to one end of the sample, while the other downstream end of the sample was at atmospheric pressure. A differential pressure applied was in the range 0.02–1.5 MPa, and the argon flow rate was measured with a mass flow meter (one in the range 0–5.10^{-3} L/min, or another in the range 0–0.3 L/min). The Klinkenberg gas slippage effect was corrected (Klinkenberg, 1941; Tanikawa & Shimamoto, 2009). Note that sample 5 was not measured for permeability because it was too damaged. Permeability data are presented in milliDarcy (1 mD = 10^{-15} m^2).

3.4. Pore Space Mapping Using ^{14}C-PMMA Method

The petrophysical parameters of the peak-ring rocks being function of the architecture of the rock porosity, a preliminary study was undertaken to map the connected pore space of two impacted granites having two different

degrees of deformation. Sample 12 has undergone intense brittle deformation, presenting crenulated foliations, and cataclasite at the microscopic scale while sample 14 is not intersected by shear faults.

The ^{14}C-PMMA (polymethylmethacrylate) method was chosen because it allows to obtain a quantitative 2D porosity mapping for all the connected pores (from nm to cm) on a multicentimeter-sized sample (Hellmuth et al., 1993). The ^{14}C-PMMA method was applied in the University of Helsinki (Finland). The two samples were dried at 55 °C for 14 days and then impregnated with ^{14}C-MMA for 6.5 months. After polymerization, the samples were cut and the sections were polished (more details are given in Siitari-Kauppi (2002) and Sardini et al. (2009, 2015)). The monomer used had a nominal activity $A0 = 274$ kBq/ml. The connected porosities were calculated using film autoradiograph (Biomax MA, Kodak) of the sections. The films were digitized using a desktop transmission light scanner Microtek Artix scan F1 (8-bit mode, pixel size 10.58 µm). Total connected porosities were calculated on the whole studied sections. Porosities were also determined on regions of interests (ROI) of sections such as primary minerals, or deformation figures.

3.5. *P* Wave Velocity

Rock seismic velocities of compressional waves (V_p) were measured at the University of Montpellier. Measurements were performed at ambient temperature (~20 °C) and atmospheric pressure using coupled piezoelectric, a pulse generator, and a digital oscilloscope. *P* wave velocities were obtained on dry and saturated samples at a 500 kHz ultrasonic frequency (wavelength of a few mm). These new *P* wave velocities are not described in Section 4 as equivalent expedition data have been extensively described and discussed in previous publications (Christeson et al., 2018, 2021; Morgan et al., 2016), but presented in Table 1 and referred to in Section 5.2 when comparing Chicxulub granite to other granitoid rocks from the literature.

4. Results and Interpretation

All measurements except for ^{14}C-PMMA are presented in Table 1, Figures 2 and 3. Sample 5, an impact melt rock, was damaged after electrical measurements, preventing the acquisition of permeability data. ^{14}C-PMMA porosity mapping is presented in Figure 4.

4.1. Density and Porosity

Figure 2 compares shipboard discrete porosity and density (OSP MAD) data and this study's data. Both data sets follow the same trend, but the porosity and densities measured by the triple weight method are, respectively, lower and higher than shipboard data. This observation supports numerical models of the formation of the Chicxulub crater (Rae et al., 2019a), which found that predicted porosities in the peak ring (7 ± 2%) were lower than the porosities indicated by OSP MAD data (14.3 ± 8%, consisting of 70% of shocked granite samples with an average porosity of 10.4 ± 2.7%). Measurements made on granite samples selected for this study sit between these values (9.6 ± 2.9%). The average bulk and grain densities of the granites are 2.47 and 2.63 g/cm^3, higher than the expedition data set (2.42 and 2.61 g/cm^3). Differences between expedition OSP measurements and this study could be due to the control of saturation and drying of the samples between the two methods used. The porosity column in Figure 2 also includes a porosity model (Clifford, 1993) used by Abramov and Kring (2004). This model is discussed in Section 5.3.

Porosity and bulk density measured on the suevites range from 8.00% to 31.53% and 2.08–2.6 g/cm^3, and they can be separated into two groups corresponding to the units they have been collected from. Suevites collected in Unit 2 have higher porosity (25.56–31.53%) and lower bulk density (2.08–2.22 g/cm^3) than two of the suevite samples 26 and 28 collected from Unit 4 (8.00–11.35%, 2.5–2.6 g/cm^3). These differences in values are interpreted to be due to different fabrics, with higher porosities and lower densities resulting from grain-supported and clast-supported fabrics (Unit 2), which is not the case in the melt-rich suevite from samples 26 and 28 (Unit 4). Note that sample 25 is also a suevite that occurs in Unit 4, but with a rather mixed and complex fabric that integrates a majority of granitic target rocks. This mixed composition is reflected by porosity and density (16.35%, 2.35 g/cm^3) values sitting between the suevites from Unit 2 and the two other suevites from Unit 4 (Figure 3a).

The porosity and density values in the suevite samples can be compared (see Figure 3a) to data collected from suevites of the onshore ICDP well Yaxcopoil-1 (Yax-1; Elbra & Pesonen, 2011; Mayr et al., 2008a) found between

Journal of Geophysical Research: Solid Earth
10.1029/2021JB023801

Table 1
Results

Sample number	Core - Section	Depth [mbsf]	Lith.	Unit [a]	Unit [b]	ϕ [%]	ρ_b [g/cm^3]	ρ_g [g/cm^3]	k (P_{eff} = 10 Mpa) [mD]	k (P_{eff} = 40 Mpa) [mD]	F	m	τ^2	C_s [mS/m]	V_p dry // sat [km/s]	IGSN
1	45-2	633.17	suev.	2	suev	31.16	2.08	2.57	2.4	7.3E-1	13.3	2.22	4.14	30.4	2.9 // -	IBCR0364EXPK301
2	54-2	660.28	suev.	2	suev	31.53	2.07	2.57	4.3E-1	1.8E-1	13.5	2.26	4.26	24.7	3.4 // -	IBCR0364EX3U301
3	62-2	683.09	suev.	2	suev	25.56	2.22	2.64	3.4E-1	2.4E-2	22.3	2.27	5.70	69.2	4.3 // 3	IBCR0364EXO3401
4	88-2	723.93	melt	3	UIM	13.16	2.47	2.70	4.6E-3	6.8E-4	150.6	2.47	19.82	7.3	5 // 4.7	IBCR0364EXNM401
5	92-2	736.31	melt	3	UIM	17.95	2.42	2.44	damaged	damaged	151.6	2.92	27.21	4.1	4.9 // 4.8	IBCR0364EXER401
6	97-2	751.45	gran.	4		8.28	2.50	2.63	1.2E-1	8.1E-2	103	1.86	8.53	1.0	3.9 // 5	IBCR0364EXIY401
7	100-2	759.03	cata.	4	UIM	18.40	2.35	2.66	5.7	3.5	25.4	1.91	4.67	2.4	2.6 // 3.7	IBCR0364EXX0501
8	103-3	768.31	gran.	4		16.66	2.33	2.59	7.8E-1	5.5E-1	20.9	1.70	3.48	0.3	3.3 // 3.3	IBCR0364EXQ2501
9	109-2	785.14	gran.	4		8.31	2.49	2.62	1.1	7.3E-1	68.9	1.70	5.73	0.3	3.2 // 4.2	IBCR0364EXC7501
10	114-2	800.67	gran.	4		8.27	2.50	2.63	6.5E-1	4.3E-1	59.8	1.64	4.95	0.6	3.6 // 4.3	IBCR0364EXS9501
11	115-2	803.54	gran.	4		12.79	2.40	2.61	5.1	3.3	31.6	1.68	4.04	0.	- // 3.5	IBCR0364EXIA501
12	122-2	819.54	gran.	4		16.39	2.36	2.63	5.9	4.7	24.3	1.76	3.98	2.3	2.8 // 3.4	IBCR0364EX9F501
13	130-2	834.72	gran.	4		6.95	2.52	2.63	3.3E-1	2.7E-1	101.3	1.73	7.04	0.5	3.5 // 4.5	IBCR0364EXYH501
14	141-2	857.72	gran.	4		8.07	2.51	2.64	7.2E-1	5.0E-1	101.6	1.84	8.20	0.8	- // 5.1	IBCR0364EXFP501
15	145-2	869.67	gran.	4		9.04	2.49	2.64	2.1	1.4	65.6	1.74	5.93	0.8	2.9 // 3.9	IBCR0364EX2S501
16	148-2	878.95	gran.	4		7.23	2.51	2.63	1.5	7.8E-1	70	1.62	5.06	0.3	3.6 // 5.1	IBCR0364EXHU501
17	156-2	901.22	gran.	4		9.82	2.46	2.62	6.7	3.6	77.4	1.87	7.60	0	- // 3.7	IBCR0364EXBZ501
18	158-2	907.36	gran.	4		10.06	2.47	2.63	7.1	4.1	39.9	1.60	4.01	0	- // 4	IBCR0364EXG0601
19	187-2	983.45	gran.	4		9.27	2.46	2.61	2.2	1.1	64.4	1.75	5.97	0.8	- // 4.4	IBCR0364EXHJ601
20	188-3	987.45	gran.	4		7.17	2.50	2.62	2.8E-1	1.3E-1	102.8	1.76	7.37	0.1	- // 4.8	IBCR0364EXXJ601
21	197-3	1015.11	gran.	4		11.60	2.44	2.63	3.0	1.6	30.9	1.59	3.58	0.8	2.7 // 4.9	IBCR0364EX1P601
22	207-2	1040.53	gran.	4		7.25	2.50	2.62	2.9E-1	1.5E-1	92.7	1.73	6.72	0.5	3.4 // 4.7	IBCR0364EXWV601
23	254-2	1183.33	gran.	4		7.31	2.51	2.63	8.6E-1	5.0E-1	83.8	1.69	6.13	1.0	3.5 // 4.6	IBCR0364EXOO701
24	274-2	1244.89	gran.	4		9.56	2.46	2.61	1.0	7.3E-1	47.6	1.64	4.55	1.4	4.7 // 5.2	IBCR0364EXE5801
25	275-2	1247.81	suev.	4	LIMB	16.35	2.35	2.62	5.9E-1	4.9E-1	28.6	1.85	4.68	1.8	3.4 // 4.1	IBCR0364EXR5801
26	281-2	1266.03	suev.	4	LIMB	8.00	2.60	2.73	5.2E-3	2.2E-4	377.1	2.35	30.17	2.2	4.8 // 5	IBCR0364EXB7901
27	290-2	1292.68	melt	4	LIMB	8.65	2.50	2.64	1.7E-3	1.5E-4	221.6	2.21	19.17	4.2	4.9 // 4.9	IBCR0364EXFE901
28	294-2	1305.26	suev.	4	LIMB	11.35	2.50	2.69	3.1E-3	1.9E-4	148.9	2.30	16.90	4.5	4.8 // 4.9	IBCR0364EXLH901
29	296-2	1311.82	gran.	4		7.64	2.50	2.63	3.5E-1	1.8E-1	81.2	1.71	6.20	1.0	3.4 // 4.3	IBCR0364EXTJ901

Note. ϕ—porosity, ρ_b—bulk density, ρ_g—grain density, k—permeability, F—formation factor, m—cementation exponent, τ^2—tortuosity, C_s—surface conductivity, V_p—acoustic velocity of compressional waves. Uncertainty for porosity, density, permeability, velocity, and conductivity is 5%. Uncertainty for formation factor, cementation exponent, and tortuosity is 8%.

[a]After Morgan et al. (2017). [b]After de Graaff et al. (2021; UIM-upper impact melt rock unit, LIMB-lower impact melt rock-bearing unit) and Kaskes et al. (2021).

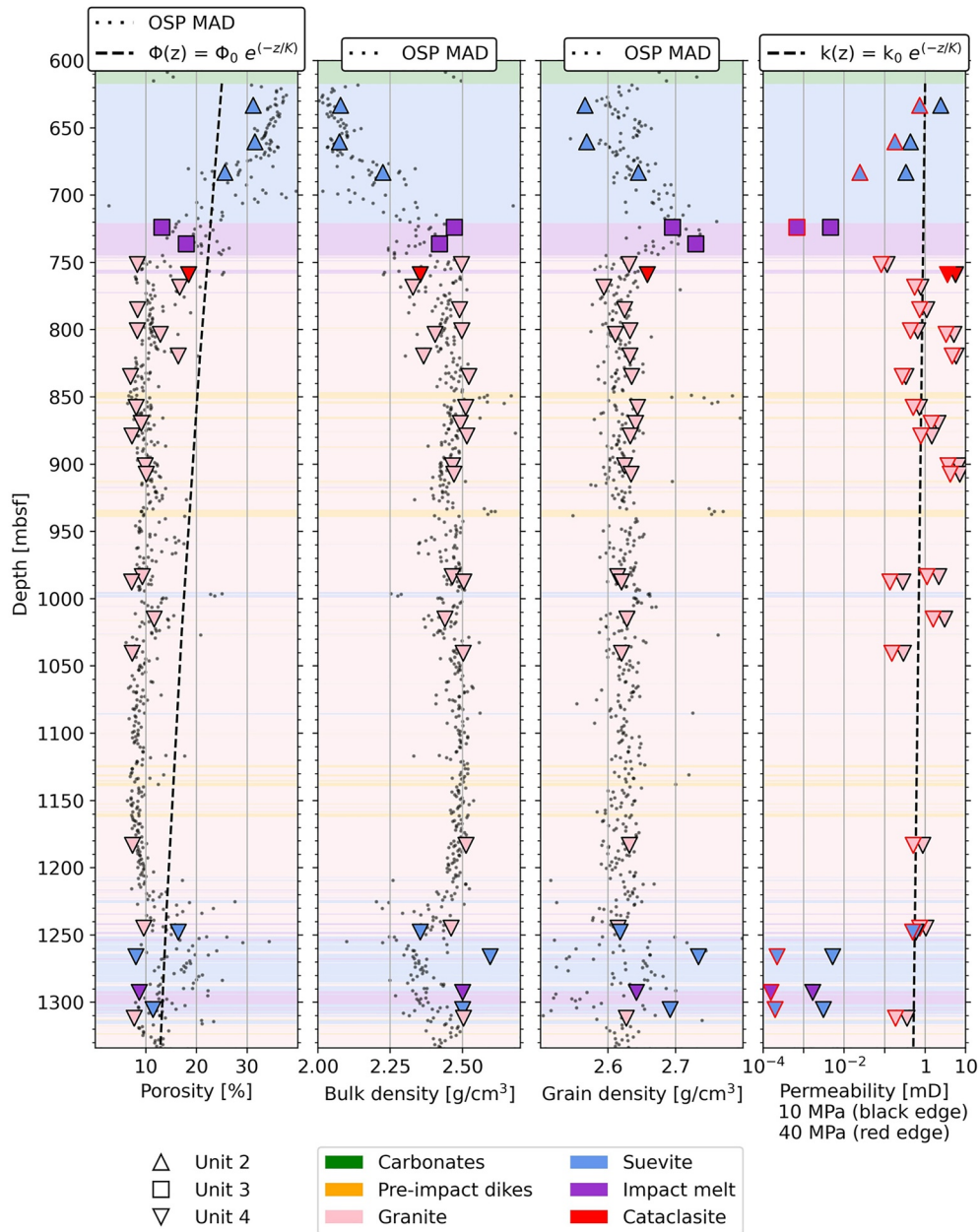

Figure 2. Porosity, bulk density, grain density, and permeability. Porosity and densities are plotted with expedition data (OSP MAD) for comparison. Permeabilities were measured at two different effective pressures (10 MPa, displayed with a black edge; 40 MPa, displayed with a red edge). Porosity and permeability models (dashed lines are plotted as $\phi(z) = \phi_0 \times e(-z/K)$ and $k(z) = k_0 \times e(-z/K)$; Clifford, 1993) are plotted after Abramov and Kring (2004) with $K = 1.07$, $\phi_0 = 25\%$, $k_0 = 1$ mD and $z_0 = 0$ shifted to 617 mbsf in the case of M0077A, the top of the peak ring). Figure designed using Python (pandas, matplotlib, and numpy).

preimpact and postimpact carbonates. In Yax-1, the lowermost impact melt rock-bearing units have lower porosities (1.95–13.1%) and higher densities (2.34–2.64 g/cm^3) compared to suevites higher in the sequence (16.6–36.8%, 2.05–2.36 g/cm^3; Mayr et al., 2008a). A similar observation can be made in Hole M0077A where suevite samples from Unit 4 have lower porosities and higher densities than suevites from Unit 2. This may reflect different depositional processes between the lowermost and uppermost melt-bearing units, both in the case of Yax-1 (Kring et al., 2004; Wittmann et al., 2007) and in M0077A (de Graaff et al., 2021; Kaskes et al., 2021), wherein the lowermost suevite intervals (or the lower impact melt rock-bearing unit (de Graaff et al., 2021) were produced

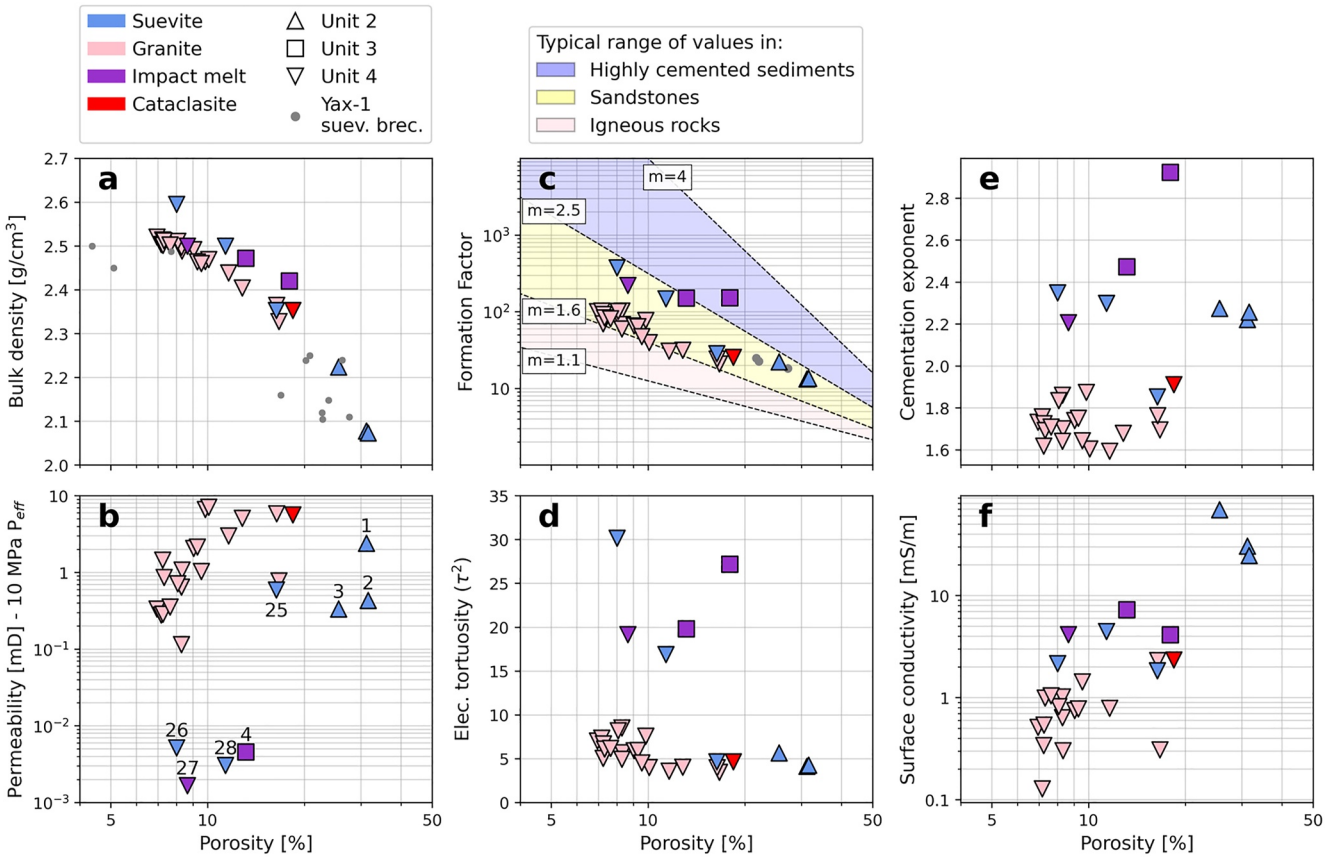

Figure 3. Summary of physical properties. (a) Porosity versus density. Note that Yax-1 data points represent average values for the different suevite units (Elbra & Pesonen, 2011; Mayr et al., 2008a) from the onshore hole Yaxcopoil-1. (b) Porosity versus permeability. Only permeabilities at 10 MPa of effective pressure are plotted. Points marked with numbers correspond to suevite and melt rock samples. (c) Porosity versus formation factor. Colored areas are for reference, giving an overview of the range of expected values for other lithologies, based on the cementation exponent m from Archie's laws (1942) where $F = \phi^{-m}$. Where $1.1 < m < 1.6$ (pink area) is typical of fractured crystalline rocks; $1.6 < m < 2.5$ (yellow area) is typical of sandstones; $m > 2.5$ (blue area) is typical of highly cemented sedimentary rocks. Gray points are Yax-1 suevite from Mayr et al. (2008b). (d) Porosity versus electrical tortuosity. Where $\tau^2 = F \times \phi$. (e) Porosity versus cementation exponent m, following Archie's law (1942), where $F = \phi^{-m}$. (f) Porosity versus surface conductivity. Figure designed using Python (pandas, matplotlib, and numpy).

in an early stage of the excavation flow, while suevites in higher intervals are more characteristic of airborne and waterborne debris and the collapse of an ejecta plume (Kaskes et al., 2021). In the case of M0077A, Unit 2 suevite is likely an equivalent to the fallback of the upper suevite in Yax-1, although Unit 2 suevite was also affected by ocean currents (Gulick et al., 2019). Suevite of Unit 4 is part of an imbricate thrust zone, interspersed with impact melt rock within the target rock (Riller et al., 2018), and the result of an earlier stage of crater formation when impactites were buried by a central uplift that collapsed to form the peak ring (de Graaff et al., 2021; Kring et al., 2017; Riller et al., 2018). Beyond this crater, Popov et al. (2014) synthesized porosity values from other impact structures, from which suevitic lithologies show a similar range of values, with average values between 7.4% and 27.9%.

Impact melt rocks from Units 3 and 4 have porosities (8.6–17.9%) and densities (2.4–2.7 g/cm^3) that compare well with the lowermost suevite of Unit 4 (8–16.3%, 2.3–2.5 g/cm^3). Sample 7 from the contact of impact melt rock and granitoid rock, where cataclasite and granite coexist, has a porosity of 18.4% and density of 2.35 g/cm^3, intermediate between suevite and granitoid rock elsewhere in the core.

Granite porosity and density values are 6.9–16.6% and 2.3–2.5 g/cm^3, respectively. Two granite samples (8 and 12) occur in more sheared, crenulated intervals than the others. Both those samples have a porosity of ~16%, which is greater than the values in other Chicxulub granites (that together without these two samples average an 8.7% porosity), and is closer to suevite and cataclasite values.

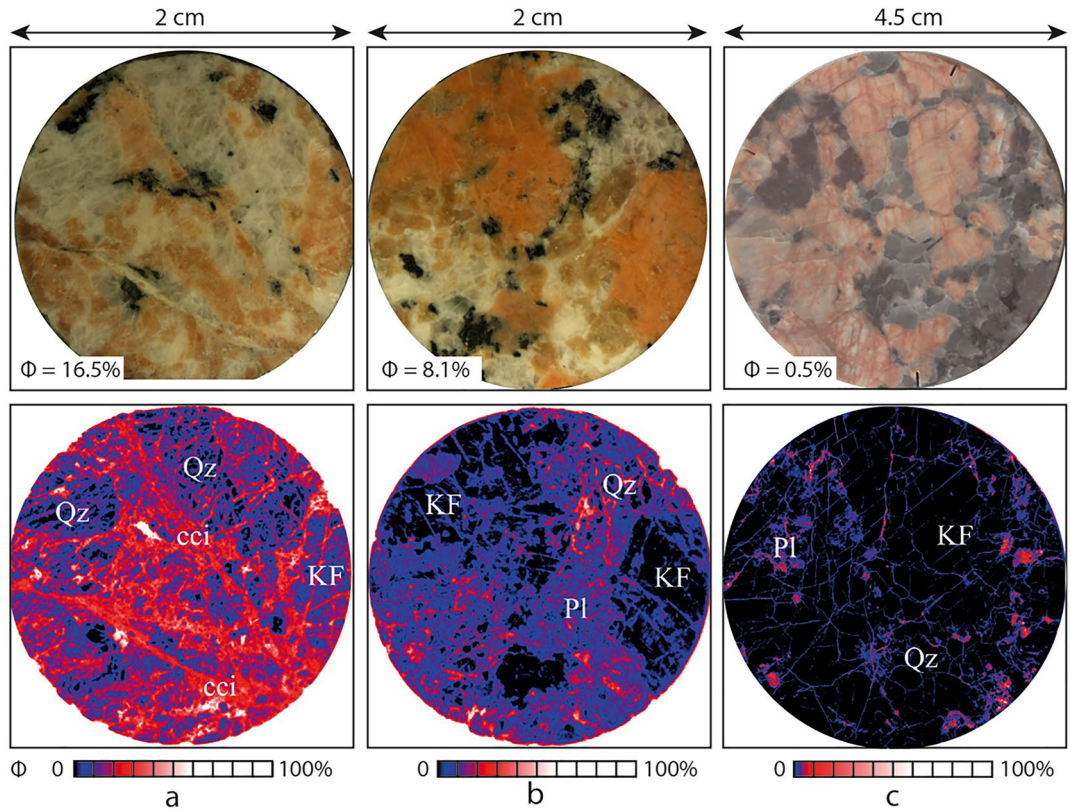

Figure 4. Samples (upper row) and corresponding porosity maps (lower row) of granitoid rocks. (a and b) Samples 12 and 14 from this study. (c) Palmottu granite. The color scales of Chicxulub samples are the same, but the one used for Palmottu granite was adapted for observing the low porosity of the rock (0.5%). Sample diameters: 2 cm for Chicxulub granite, and 4.5 cm for Palmottu granite. Qz, quartz; Pl, plagioclase; KF, K-feldspar; cci, cataclasite.

4.2. Porosity Mapping

The porosity maps obtained for the two studied granitoid rock samples do not present any artifacts due to the method itself; it is assumed that the connected porosity of these samples was totally impregnated using the experimental protocol. This assumption was verified by calculating the total connected porosity of these samples using ^{14}C-PMMA method. The total porosities of the two impregnated granites obtained from ^{14}C-PMMA method are 16.5% and 8.1% for samples 12 and 14, respectively. These values are similar to the ones determined by the triple weight method (Table 1): 16.4% and 8.1% for samples 12 and 14, respectively. Porosity maps obtained for these two samples look very different (Figures 4a and 4b) and are compared for reference with an intact granite (Palmottu granite; Figure 4c).

The main visible feature on the porosity map of sample 12 is the occurrence of cataclasite and shear faults transecting the samples. These shear faults are more porous than the average porosity of the sample (average porosity of the shear faults determined on ROI is 26.2%). These bands are made of an assemblage of small clasts (clasts size ranging from mm to <μm) and a matrix which is difficult to resolve by Scanning Electron Microscopy. Due to their small size, it is not possible to separate the porosity of these clasts from the matrix using the ^{14}C-PMMA method. At a greater scale of investigation, this sample contains large quartz (average porosity 7.7%) and K-feldspar aggregates (average porosity 14%), crosscut by transgranular fractures which are well visible by autoradiography. Plagioclase are rare in this sample. This sample also contains macropores (pore size >500 μm), which are associated with dark mineral aggregates (biotite/chlorite assemblage, average porosity 71.4%).

Sample 14 does not present shear faults and has an appearance closer to the majority of granitoid rock samples recovered in Hole M0077A. Four mineral aggregates are present (K-feldspar, plagioclase, quartz, and dark minerals), as described in Morgan et al. (2017). The porosities of these aggregates are quite contrasted as determined on ROI: K-feldspar 1.9%, plagioclase 10.6%, quartz 10.6%. The dark minerals are ignored here because of their

relatively low abundance. K-feldspar is a relatively lowly porous mineral in this sample, the main 3D connected porosity of this rock being formed by the quartz/plagioclase aggregates, as already reported by Rae et al. (2019a). Quartz and plagioclase can be distinguished in the autoradiography. The only porosity observed in quartz is due to transgranular fractures. The plagioclase is very densely cracked, but the fractures are not well resolved by autoradiography because their density is too high. The high porosity found in plagioclase aggregates (10.6%) can thus be mainly attributed to crack porosity.

4.3. Permeabilities

At an effective pressure (P_{eff}) of 10 MPa, which corresponds roughly to the pressure at the top of the submerged peak ring soon after impact, clast-supported suevites from Unit 2 together with the high-porosity, granite-rich suevite (sample 25) from Unit 4 have similar permeability values (0.3–2.4 mD). These are 2–3 orders of magnitude higher than melt-rich suevites and impact melt rocks from Units 3 and 4 (1.7×10^{-3}–5.2×10^{-3} mD). These two groups of samples (1, 2, 3, 25 and 4, 26, 27, 28) form two clear clusters in Figure 3b. Granites have rather high permeabilities (0.1–7.1 mD), comparable to the clast-supported suevites from samples 1, 2, 3, and 25, despite having lower porosities, that are comparable with melt-rich suevites and impact melt from samples 4, 26, 27, and 28. The mixed cataclasite and granite sample (sample 7) also have a relatively high permeability of 5.7 mD.

Apart from the melt-rich samples (4, 26, 27, and 28), other lithologies have permeabilities of 10^{-1}–1 mD that compare with values typically measured in sandstones, volcanic rocks or limestones for similar porosity ranges (Brace, 1980; Schön, 2015) at $P_{eff} < 10$ MPa. Granite samples, as well as samples rich in granites (7 and 25) also show a limited sensitivity to increasing P_{eff} from 10 to 40 MPa (Figure 2, fourth column and Figure 6), with permeability rarely decreasing by 1 order of magnitude. Permeability of granitoid rocks is further discussed in Section 5.2. Values are consistent with previous hydrothermal models for Chicxulub crater and peak ring that considered surface permeabilities of 10^{-1}, 1, and 10 mD (e.g., Abramov & Kring, 2007), and are discussed in Sections 5.1 and 5.3.

4.4. Electrical Properties

In the clast-supported, high-porosity suevites from Units 2 and 4 (samples 1, 2, 3, and 25), F is between 10 and 30, 10 times lower than in melt-rich suevites and impact melts from Units 3 and 4 (samples 4, 26, 27, and 28; Figure 3c). The former has porosities and formation factors both comparable to suevitic breccia from Yax-1 (Mayr et al., 2008b) and also compare well with the mixed granite-cataclasite sample ($F = 25$). Except for the granite-rich suevite sample 25, the cementation exponent in the suevites and impact melt rocks ranges between 2.2 and 2.9, averaging 2.3 (Figures 3c and 3e). In granites, formation factors range from ∼20 for the more porous samples to ∼100 for the less porous samples. The average cementation exponent is 1.7 (ranging from 1.59 to 1.87). Samples 7 (granite/cataclasite) and 25 (granite-clast-dominated suevite occurring near a melt interval) have cementation exponents (1.91 and 1.85, respectively) closer to granites than suevites or impact melt rocks.

Electrical tortuosity is below 10 in all samples except in the melt and melt-rich suevites (samples 4, 26, 27, 28), where it is between ∼15 and ∼30. Above a porosity of 10%, the tortuosity of the granites remains between ∼3.5 and ∼4, it tends to be more scattered between ∼4.5 and ∼8.5 with lower porosities (Figure 3d).

Surface conductivities C_s (Table 1 and Figure 3f) are typically higher in the three suevites from Unit 2, with values between 25 and 69 mS/m. Impact melt rocks and other suevites (and the granite/cataclasite sample 7) have values between 4–7 and 1.8–4.5 mS/m, respectively. Granites have lower values close to 1 mS/m, except for sample 12, which has a value of 2.3 mS/m.

5. Discussion

5.1. Physical Properties of the Peak Ring

In petrophysics, the cementation exponent (m), calculated from the formation factor and the porosity, reflects the porosity microgeometry and the degree of cementation of rocks. It can roughly be divided into three main domains. Archie (1942) first observed that m typically ranged between 1.8 and 2 in consolidated sandstones. Glover et al. (1997) and Revil and Cathles (1999) synthesized values of m to fall between 1.5 and 2.5 in sandstones.

Lower ranges of m values, from 1.1 to 1.6, are generally measured in fresh igneous rocks (Belghoul, 2007) as a signature of a well-connected porosity through microfractures and/or microcracks. Finally, higher m values (e.g., $m > 2.5$) are observed in rocks with a poorly connected porosity such as highly cemented sandstones and vuggy carbonates.

In the present study (Figure 3e), granites and samples 7 (cataclasite/granite) and 25 (granite-rich suevite) have cementation exponents (1.6–1.9) that are not typical of fractured crystalline rocks ($m < 1.6$). They are closer to values observed in consolidated sandstones ($1.5 < m < 2.5$). The two granite samples impregnated by ^{14}C-PMMA have a cementation factor of 1.76 (sample 12) and 1.84 (sample 14), falling in the category of consolidated sandstone. These unusually high values of m can be qualitatively explained by the spatial distribution of pore space. Pore space of these rocks is not at all similar to fresh or deformed granites previously investigated such as Palmottu granite, Finland (Oila et al., 2005; Figure 4). The high porosities of these shocked samples stems from the impact-derived structures (shear faults, microcracks). Although present, microcracks are not the main connected structures of sample 12. The presence of large, and porous shear faults crosscutting the sample, forming cataclasites, modifies the connectivity of pore space, and influences the value of m compared to a fresh granite. For sample 14, it was observed that plagioclase/quartz aggregates contain a dense network of intragranular cracks. Thus, these polymineral aggregates form the main continuous porous network through the rock. This porous aggregate is so densely microcracked that it can be suggested that it behaves as a cohesive or moderately cemented clastic rock, as reflected by their cementation exponents. The three clast-supported suevites from Unit 2 have higher cementation exponents (2.2–2.3) than the granite samples, typical of a highly cemented sandstone. Finally, the rest of the (melt-rich) suevites (samples 26 and 28) and the three impact melt rocks (samples 4, 5, and 27) have the highest cementation exponents (2.2–2.9), reflecting the least connected porosity. These five melt-rich samples also happen to have higher electrical tortuosity.

Electrical tortuosity (τ^2), also calculated from the formation factor and the porosity, reflects more the complexity of the path followed by the electrical current (Ildefonse & Pezard, 2001). Samples fall into two ranges of values, melt-rich samples have higher tortuosity (>15) than all other samples (<10; Figure 3d). It means that according to the measurements performed on the samples, electrical current travels less efficiently in melt-rich lithologies, likely as a result of a more complex, less connected pore network compared to granites and clast-supported suevites. This is also reflected by the lower permeabilities observed in the melt-rich lithologies. These observations suggest that, at the matrix scale and open fractures aside, impact melt rocks cutting through the peak ring may have acted like a barrier that stopped, deviated, or slowed the fluid flow within the formation below the crater. On the other hand, the granite and grain-supported suevites were and still are relatively more porous and more permeable lithologies. The electrical tortuosity, function of porosity, of granite sample 14 (8.20) was found to be significantly higher than that of sample 12 (3.98). The path followed by the electric current is probably less complex in sample 12 due to the presence of porous shear faults crosscutting the whole sample (Figure 4). The same conclusions are valid for fluid flow, permeability of sample 12 being 1 order of magnitude higher than permeability of sample 14 (Table 1).

That finding has important implications for models of hydrothermal flow. While individual rock units may have permeabilities of 1–10 mD, a representative permeability for the entire system, which accommodates barriers to flow like that of impact melt rocks, may be closer to 0.1 mD. Thus, future models may need to adjust permeability values depending on the scale being modeled. If a model is addressing circulation in the uppermost 100 m of the peak-ring sequence, then permeabilities of order of 1 and 10 mD are appropriate. If a model is addressing circulation for depths of 1 km or greater, then a permeability of order 0.1 mD may be appropriate. This observation is, strictly speaking, limited to the peak-ring section sampled at site M0077A. Other types of crater heterogeneities should be explored in future models, possibly implementing a layered approach to account for potential barriers cutting through the shocked target rocks.

The surface conductivity measured in the 19 granitoid rock samples is low, this indicates that there are a few altered minerals present in these samples, possibly cleared out by fluid circulation after the hydrothermal process, or that altered minerals are poorly conductive. Suevites and impact melt rocks have higher surface conductivity because they contain more altered minerals, principally smectites which were well characterized from geochemical analysis as part of IODP-ICDP Expedition 364 (Morgan et al., 2017; Figure F21; see also Simpson et al., 2020). The granite was affected by hydrothermal alteration after the impact (Kring et al., 2020; Morgan et al., 2017).

Table 2
Granitoid Rock Formations Used to Compare Physical Properties

Granitoid rock formation	Study/site	Sample	Alteration	Reference
Barre	Research on nuclear waste storage, research on hydraulic properties	Core from block	Intact	Kranz et al. (1979)[c] and Owens (1979)[b]
Chelmsford	Research	Core from block	Intact	Bernabe (1988)[b,c]
Grimsel	Research on nuclear waste storage	Core from tunnel	Shear zone	Schild et al. (2001)[b,c]
		Core from tunnel	Intact	David et al. (2018)[b,c]
Illinois	Research	Core (700–1,600 mbgl)	Intact	Morrow and Lockner (1997)[b,c]
Nojima	Fault zone	Core (200–750 mbsf)	Intact to altered	Pezard et al. (1999b)[b]
		Core from outcrops (Funaki and Hirabayashi)	Intact to altered (fractured, breccia, cataclasite (cci))	Mizoguchi et al. (2008))[c]
Palmottu	Research on nuclear waste storage	Core (<100 mbgl)	Intact	Oila et al. (2005)[a] and Sardini et al. (2007)[a]
La Peyratte	Research	Core from block	Thermally and mechanically cracked	David et al. (1999)[b]
Ploemeur	Fractured aquifer	Core (<100 mbgl)	Intact to hydrothermally altered	Belghoul (2007)[b]
Poitou	Research on nuclear waste storage	Core (200–600 mbgl)	Intact to hydrothermally altered	Belghoul (2007)[b] and Pezard et al. (1999a)[b]
Soultz	Geothermal energy	Core (1,400–2,200 mbgl)	Intact to hydrothermally altered	Géraud et al. (2010)[b] and Rosener (2007)[b]
Takidani	Research	Core from block	Intact	Benson et al. (2006)[c]
Westerly	Research	Core from block	Intact and thermally cracked	Brace (1977)[b], Brace et al. (1968)[c], Nasseri et al. (2009)[c], and Nur and Simmons (1969)[b]

Note. Samples from Nojima (Pezard et al., 1999b), Ploemeur, and Poitou shown in Figure 5 were all analyzed following the same methods as the ones used in this study. mbsf, meters below sea floor; mbgl, meters below ground level.
[a]Used in Figure 4. [b]Used in Figure 5. [c]Used in Figure 6.

5.2. Comparing the Chicxulub Granite With Other Granitoid Rocks

In order to characterize to which degree the target rocks from Chicxulub's peak ring have been affected, collected data are compared with similar measurements on physical samples from other granitoid rocks from the literature (Table 2, Figures 4, 5, and 6). Selected granitoid rocks cover intact formations from the surface and from borehole, as well as formations modified by natural processes (faults, hydrothermal activity) or lab experiments. In Figure 5, porosity data from Chicxulub samples and other granites are plotted against, when available: bulk density, formation factor, permeability, tortuosity, and surface conductivity. Values for the samples from the Poitou have been averaged by depth intervals of similar lithologies/alteration (intervals typically <3 m) owing to the large number of total measured samples (>60) that would clutter the plots. For Soultz samples (Géraud et al., 2010) if several measurements exist for one sample or depth, they have been averaged. Overall, Chicxulub samples have values that are outside the ranges of other granitoid rocks, intact, or altered.

Of the selected granitoid rocks shown in Table 2, only a 40-cm thick interval of heavily hydrothermally altered Poitou tonalite, from which were measured 11 samples, has porosities (8.54–15.95%) and formation factors (40–306) comparable to Chicxulub granites. Values from this interval have been averaged into one point (ϕ = 10.8%, ρ_b = 2.51, F = 97, τ^2 = 9.5, C_s = 23.3 mS/m) shown in Figures 5a, 5c, 5d, and 5e. However, the surface conductivity of this granitoid rock interval (5.7–37.9 mS/m) averages 23.3 mS/m, it is higher than the surface conductivity measured on Chicxulub shocked granites (<2.7 mS/m). In this interval from the Poitou, except for quartz, the original matrix and later veins are pervasively replaced and filled by sericite and chlorite. In fact, samples from this interval were so altered that the majority were partially destroyed after being dried then resaturated multiple times in the process of calculating F and C_s. Chicxulub granite underwent hydrothermal alteration (Kring et al., 2020; Timms et al., 2020) but not as extensively as this granitoid rock from the Poitou. In

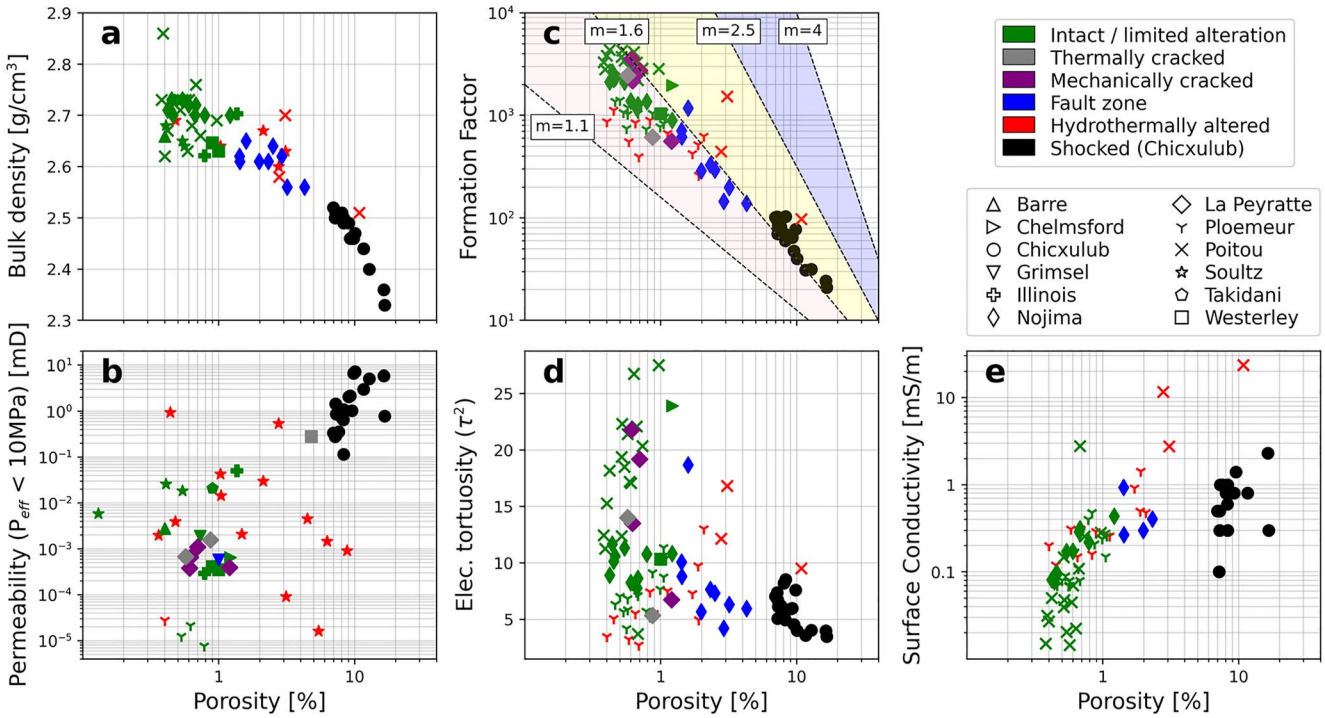

Figure 5. Comparison of physical properties between different granitoid rock formations. Marker shapes correspond to granitoid rock formations (see Table 2), and associated colors to different types of alterations. (a) Porosity versus bulk density. (b) Porosity versus permeability. (c) Porosity versus formation factor. Dashed lines are for reference, giving an overview of the range of expected values for other lithologies, based on the cementation exponent m from Archie's laws (1942) where $F = \phi^{-m}$. Where $1.1 < m < 1.6$ (pink area) is typical of fractured crystalline rocks; $1.6 < m < 2.5$ (yellow area) is typical of sandstones; $m > 2.5$ (blue area) is typical of highly cemented sedimentary rocks. For Chicxulub granite samples, m ranges from 1.59 to 1.87, for a mean value of 1.71. (d) Porosity versus electrical tortuosity, where $\tau^2 = F \times \phi$. (e) Porosity versus surface conductivity. Figure designed using Python (pandas, matplotlib, and numpy).

the peak ring, hydrothermal alteration is principally observed near the contacts between melt zones and granites (e.g., samples 6 and 29), and along cracks, yet no complete replacement of the original minerals was observed. The granite preserved most of its original texture and its unusual physical (and resulting electrical) properties are interpreted to be impact-induced (e.g., shock metamorphism, dynamic collapse of the peak ring; Rae et al., 2019a, 2019b).

From all the plotted granitoid rocks in Figure 5b, only two Soultz samples and one cracked Westerly sample show similar range of permeability (>10^{-1} mD), comparable to Chicxulub samples under $P_{\text{eff}} < 10$ MPa. The Soultz samples are fractured (Rosener, 2007) in addition to being hydrothermally altered, explaining the high permeability values. For the Westerly granite, cracks were formed by heating it up to a temperature of 850 °C (Nasseri et al., 2009). The effect of increasing P_{eff} on permeability on that same sample is shown in Figure 6 (right—Westerly—850 °C). In comparison with Chicxulub samples that have a similar permeability range of values under low stress, cracks causing high permeability in the Westerly sample tend to close with increasing P_{eff}, while Chicxulub samples remain relatively insensitive. The effect of cracks and stress on crystalline rocks is discussed in the following sections.

5.2.1. Cracks and Microcracks in Granitoid Rocks

Microcracks are the dominant form of porosity observed in granitoid rocks (see references in Table 2), Figure 5 illustrates that fresh granites tend to have a porosity mainly <1%. In fresh granitoid rocks, intragranular porosity of primary minerals is always low: plagioclase porosity ranges from 0.1% to 1.14%, quartz porosity ranges from 0.15% to 0.68%, and K-feldspar porosity ranges from 0.15% to 0.70% (Cassiaux, 2004; Kelokaski et al., 2006; Sardini et al., 2006; Voutilainen et al., 2019). When a sample porosity is <0.5%, the porosity of quartz and feldspar often falls below the detection limit of the ^{14}C-PMMA method and grain boundary porosity is dominating.

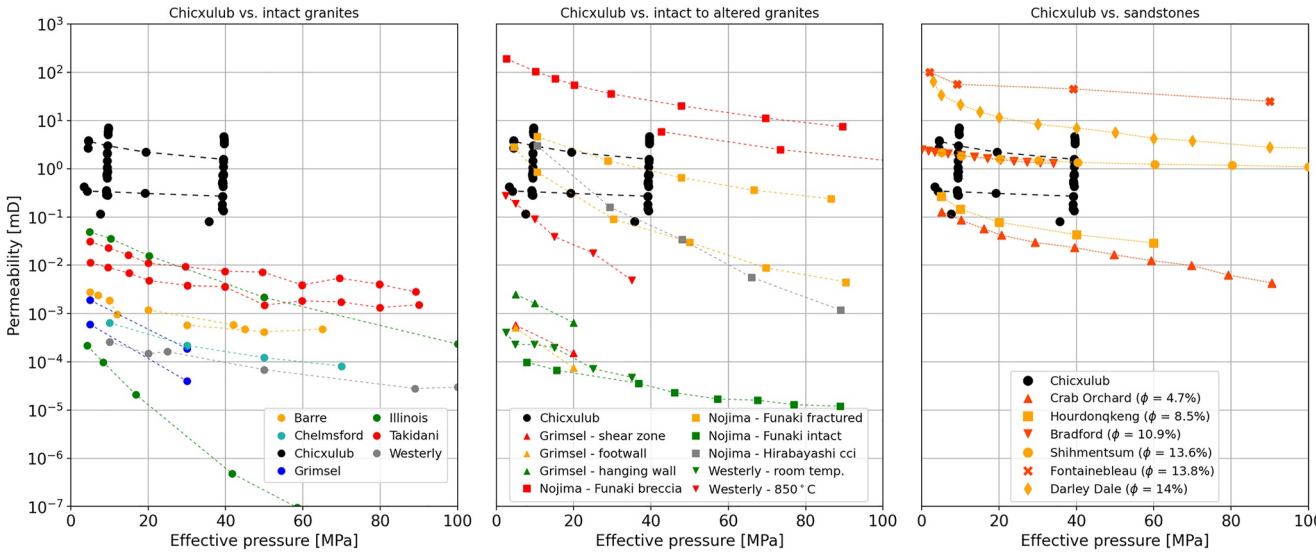

Figure 6. Permeability comparisons between Chicxulub granite and different granitoid rock formations and sandstones. Different granitoid rock formations and references are listed in Table 2. When references give multiple permeability measurements, only the minimum and maximum trends are plotted. The left panel gives examples of intact to poorly altered granitoid rocks (Barre: Kranz et al. (1979); Chelmsford: Bernabe (1988); Grimsel: David et al. (2018); Illinois: Morrow and Lockner (1997); Takidani: Benson et al. (2006); Westerly: Brace et al. (1968)). The central panel gives examples of intact to altered granitoid rocks (Grimsel: Schild et al. (2001); Nojima: Mizoguchi et al. (2008); Westerly: Nasseri et al. (2009)). The right panel compares Chicxulub granitoid rocks to sandstone formations (Crab Orchad Formation: Benson et al. (2006); Hourdonqkeng and Shihmentsum formation: Tanikawa and Shimamoto (2009); Bradford Formation: Wyble (1958) (note: *x* axis is confining pressure for this example); Fontainebleau Formation: David et al. (1994); Darley Dale Formation: Zhu and Wong (1997)). Figure designed using Python (pandas, matplotlib, and numpy).

In granitoid rocks, cracks affect brittle minerals (quartz and feldspars) the same way. For instance, the crack density observed in fresh granites like Palmottu granite (Oila et al., 2005) is quite homogeneous (Figure 4c). Palmottu granite has a mineralogy comparable to the samples from this study, and has a porosity in the classic range of fresh granitoid rocks (~0.5%). In this fresh granite, the porosity of plagioclase (1.14%), quartz (0.56%), and K-feldspar (0.48%) is quite similar (Oila et al., 2005), because the porosity of these minerals is mainly due to intragranular cracks (but plagioclase also exhibits intragranular microporosity, see porous patches in Figure 4c).

As a granitoid rock is altered, the density and aperture of cracks increases, associated with an increase in porosity. Even in naturally or artificially cracked granitoid rocks, excluding weathering, porosity rarely exceeds 5%. Chicxulub samples have a porosity of 9.6 ± 2.9%. In Chicxulub sample 14, ^{14}C-PMMA method provides a porosity of 10.6% for both quartz and plagioclase, and a much lower porosity in K-feldspar (1.9%). The porosity of these three minerals results mainly from intragranular cracks. These minerals are more porous than the maximal porosity found in different unaltered granitoid rocks synthesized above. One major specificity of Chicxulub shocked granite is the important and unexpected contrast of porosity (microcrack porosity) between quartz + plagioclase and K-feldspar. K-feldspar crystals form isolated lowly porous aggregates in a matrix about five times more porous. This difference is supposed to be inherent to the differential mechanical deformation of the rock during the cratering (Riller et al., 2018). The mineral aggregates were so affected during cratering that the porosity spatial distribution of the sample does not compare to other porosity distribution usually observed in granitoid rocks (as described in Sardini et al. (2007)). The microcrack density and associated electrical properties suggest that Chicxulub granite could be compared, e.g., to a moderately cemented sandstone in terms of porosity and formation factor. To further assess this assumption, it is interesting to observe how the samples behave in response to increasing stress during permeability measurements.

5.2.2. Effect of Stress Relief

Permeability data shown in Figure 6 compare measurements collected from the Chicxulub core samples with intact (left) and intact to altered (right) granites. When a reference gives several sets of measurements, only a

selection is plotted to reflect the range of values of the data set. Overall, permeabilities from Chicxulub's target rocks range within 0.1 to <10 mD. From 10 to 40 MPa of effective pressure (P_{eff}), the permeability of the samples decreases within the same order of magnitude as they started in. Under the same P_{eff} range, fresh granites have lower permeabilities (10^{-2}–10^{-5} mD) at 1–10 MPa, and they typically decrease by 1 or 2 orders of magnitude when reaching 40 MPa (Figure 6, left). Permeability measurements performed on samples extracted from boreholes tend to be more sensitive to increasing stress (e.g., Illinois, Grimsel), it is not the case for Chicxulub samples that were extracted from ∼750 to ∼1,330 mbsf). In other granites, Morrow and Lockner (1994, 1997) suggest that these trends are associated with the damaging of the samples during coring (thermal cracks, stress relief cracks). These damages increase the permeability compared to what it would be in situ. During laboratory measurement, as P_{eff} increases, sampling-induced cracks are closed and the permeability decreases significantly. For these samples, measurements at higher pressure may reflect in situ stress more accurately; however, permeability values may still be dominated by sampling-induced cracks as their formation is irreversible. Schild et al. (2001) also studied the effect of stress relief associated with sampling on the Grimsel granodiorite. Some of their results for samples extracted underground, in the vicinity of a shear zone, are plotted in Figure 6 (right). Other measurements on intact Grimsel granodiorite samples are plotted in Figure 6 (left), following a permeability benchmark study by David et al. (2018). Despite having been sampled in situ at depth >750 mbsf, Chicxulub specimens do not exhibit the same behavior as other granitoid rocks that underwent stress relief during sampling in situ.

Surface samples (e.g., Chelmsford, Westerly, Barre, Takidani—Figure 6 (left)) are less sensitive to changes in pressure during measurement because they did not undergo stress relief and associated crack formation, or at least not to the same extent than borehole samples, at collection. Yet, due to weathering and other surface processes, permeabilities from such samples are likely to be higher to what they would be if an intact sample was collected from a deep drillhole counterpart (Morrow & Lockner, 1994). Chicxulub granitoid rock samples are less sensitive to increasing stress than fresh granitoid rock surface samples.

5.2.3. Deformed Granitoid Rocks

Samples from a tectonically active area, the Nojima fault, have been studied both with surface samples (Mizoguchi et al., 2008) and from core samples (Lockner et al., 2009). Altered surface samples collected within 10 m from the fault core have permeability values of 1 and 10 mD (fractured granite, granitic cataclasite) and up to 10^2 mD (granitic breccia) under low P_{eff} of 5–10 MPa, these values decrease by 1–2 orders of magnitude when P_{eff} increases to 50 MPa. A selected set of data from Mizoguchi et al. (2008) is plotted in Figure 6 (right), including a fresh granite collected 100 m away from the fault. Surface Nojima fractured granites and cataclasite compare well with Chicxulub granite samples in terms of permeability values under low P_{eff}, but are more sensitive to increasing stress.

Borehole samples (Lockner et al., 2009), collected within ∼18 m from the fault, including damaged granitoid rocks (brecciated, fractured, sheared; Moore et al., 2009) have permeabilities of 10^{-3} to <10 mD under a confining pressure of 10 MPa. Although having lower permeability values than surface samples, both of these data sets overlap within a range of permeability values comparable to Chicxulub samples (10^{-1}–10 mD) under low stress. However, unlike Chicxulub granites, their permeability decreases similarly by 1–2 orders of magnitude when pressure is increased to 50 MPa. Overall, if permeability values from surface and borehole tectonized granitoid rock samples from the Nojima fault can be compared with granites from Chicxulub, the latter are relatively insensitive to increasing stress.

5.2.4. Experimentally Cracked Granitoid Rocks

Rae et al. (2019a) observed that the largest contributor to porosity in Chicxulub granites were intragranular fractures (55%), followed by intergranular pores (24%), and cataclasite (21%). Although it is challenging to reproduce stress conditions to generate similar shock-induced porosity, thermally cracked granites develop both intragranular and grain boundary cracks (Nasseri et al., 2007). Permeability measurements performed on intact and thermally cracked Westerly granite samples (Nasseri et al., 2009) are shown in Figure 6 (right). After being heated to 850 °C, the permeability of the Westerly granite is within the lower part of the range of values from

Chicxulub samples at $P_{eff} \sim 5$ MPa. However, its permeability decreases by 2 orders of magnitude when P_{eff} is increased to 35 MPa.

Thermally cracked samples are also characterized by a significant decrease in dry P wave velocities. Nasseri et al. (2007) reports values of 4.48 km/s (porosity <1%) on intact samples that drop to 0.98 km/s (porosity = 3.8%) after being heated to 850 °C. Chicxulub granite samples have an average dry P wave velocity of 3.4 km/s and an average porosity of 9.6%. Compared to granites heated at 800 °C and more, these values are >three times higher for V_p (Nasseri et al., 2007; Yang et al., 2017; Zhang et al., 2018) and >1.5 times higher for porosities (Nasseri et al., 2007, 2009; Sueyoshi et al., 2020; Yang et al., 2017; Zhang et al., 2018). Nasseri et al. (2009) point out that the aperture of the cracks and their density are important controlling factors to porosity and permeability reduction with increasing pressure. Porosity decreases more significantly in samples with lower crack density and aspect ratio than in heated samples showing higher crack density and apertures. This could suggest that the high crack density of Chicxulub granites makes them less sensitive to increasing stress compared to other granites.

5.2.5. Mechanical Behavior of Chicxulub's Granitoid Rock

For the selected granitoid rocks from the literature, decrease in permeability is typically associated with the closure of cracks and microcracks. At $P_{eff} < 10$ MPa, samples from this study have rather high permeabilities, comparable to naturally or experimentally deformed granites, but have higher porosities and appear to be relatively insensitive to increasing P_{eff} up to 40 MPa. Limited sensitivity to increasing P_{eff} can be observed in cracked rock samples as a result of fracture surface roughness and offset (e.g., Pérez-Flores et al., 2017; Sarout et al., 2017). In cataclasite zones where offsets can be observed (McCall et al., 2021; Riller et al., 2018), this phenomenon could be a contributing factor to the lack of sensitivity in response to increasing stress. However, in the rest of the shocked Chicxulub granitoid rocks, it is suggested that the pervasive fracturing fragmented the original structure of the target rock and grains without clear offset (Figures 4a and 4b; also see Figure 4 in Rae et al. (2019a)), making it behave like a moderately cemented clastic rock, as observed with electric properties. This insensitivity to increasing P_{eff} up to 40 MPa and the associated permeability values are also closer to what can be observed in clastic rock formations. For example, measurements performed on the Bradford sandstone by Wyble (1958) provide comparable porosity (9–11.6%), formation factor (56–127), and permeability (0.48–2.48 mD) values, with slightly higher cementation exponents (1.8–2.1) and tortuosity (6.3–12.3). Another example is the Fontainebleau sandstone, that for similar porosity range (6.7–12.6%), has comparable formation factors (28–130) and cementation exponents (1.3–1.87) and tortuosity (2.3–9.5; Revil et al., 2014). In the case of the Fontainebleau sandstone, however, permeabilities are up to 2 orders of magnitude higher than for Chicxulub granitoid rocks (Figure 6). Under increasing stress permeabilities of these sandstones tend to decrease within the same order of magnitude, like the shocked granite samples from this study. In terms of permeability reduction against increasing stress, other rock formations show comparable insensitivity under increasing confining or effective pressure. This is the case for volcanic rocks with porosities ranging from ~4 to >40% (e.g., Fortin et al., 2011; Heap et al., 2018; Kennedy et al., 2020; Nara et al., 2011); however, few studies combine these permeability measurements with a characterization of the porous space with electric measurements. Investigation of electrical properties on volcanic rocks ranging between 6% and 12% point at a cementation exponent m closer to the range 1.8–2.9, and tortuosity in the range 6–90 (e.g., Bernard et al., 2007; Ghorbani et al., 2018; Revil et al., 2019; Soueid Ahmed et al., 2018), overall higher than the values ($1.59 < m < 1.87$ and $3.48 < \tau^2 < 8.53$) observed on Chicxulub granitoid rocks, and therefore likely associated with a less connected porosity.

Different mechanical behavior or porous media under increasing effective pressures have been divided in three types by David et al. (1994). Crystalline rocks are Type I, the most sensitive to an increasing stress as microcracks close. Intact or deformed, most samples plotted in Figure 6 fit this Type I, except for Chicxulub samples that remain insensitive. Type II is typically observed in porous clastic rocks, where the limited decrease in permeability is dependent on adjustment of grains under increasing stress. Finally, Type III is more typical of unconsolidated materials: almost insensitive to increasing stress, until reaching a critical pressure beyond which grains start being crushed, leading to an abrupt decrease in permeability. In the present study, samples follow a Type II trend within the range of studied pressure (P_{eff} max = 40 MPa). This maximum pressure is already ~three times higher than the stress of the formation downhole, the permeability values are therefore representative of in situ

conditions. Future investigations should put the samples under higher stress to observe their behavior and the effect on permeability at greater depths; insensitivity to increasing pressure could affect hydrothermal models.

Shock metamorphism, combining high pressure and high temperature, as well as movement of the recovered section by >20 km within 10 min during the impact event (Morgan et al., 2016) resulted in the observed physical properties of Chicxulub granites. Microscopic observation of Chicxulub granite samples (Figures 4a and 4b; Rae et al., 2019a; Riller et al., 2018) point at a range of rock damaging modes (e.g., pervasive fracturing, fragmentation of the minerals and shear faulting) that result from the stress during the impact and crater formation. The shock pressure and release shattered the original texture and crystals, and eventually formed cataclasite (McCall et al., 2021; Rae et al., 2019a). The target rocks have been deformed in such a way that, at the studied scale (cm-scale samples), it could be suggested that they behave more like a cohesive or moderately cemented clastic rock than a fractured crystalline rock.

5.2.6. Other Shocked Granitoid Rocks

Shock effects on physical properties have been investigated in the Ries crater (Popov et al., 2003). These authors used a theoretical model based on thermal conductivity measurements and grain and pore geometry models to estimate the porosity of physical samples. In order to tune their model, the authors defined pores from penny-shaped cracks to spherical porous space. Following this method, granitoid rocks from this impact crater have calculated porosity values ranging from 8.60% to 23.4%, with an average of 15.2%. This average value is higher than the average value for the samples presented in this study (9.6%). Thermal conductivity data used for their calculation include measurements on saturated samples, with values ranging from 1.85 to 3.27 W m^{-1} K^{-1} (average = 2.52 W m^{-1} K^{-1}). Chicxulub granite samples have thermal conductivities on saturated samples ranging from 2.22 to 3.40 W m^{-1} K^{-1} (average = 2.72 W m^{-1} K^{-1}; Morgan et al., 2017). Higher thermal conductivity values observed in Chicxulub samples are compatible with lower porosity, compared to the Ries porosity model. Higher porosity being associated with lower thermal conductivity, as pore space slows heat transfer.

Other candidates to compare to Chicxulub's samples are granites from nuclear test sites (Boardman & Skrove, 1966; Derlich, 1970a, 1970b; Short, 1966). Intact granite samples from these test sites have V_p of 5–5.9 km/s. V_p measurements (2.9–4.5 km/s) acquired on shocked samples from the Hoggar and Hardhat granites in a range of 10–30 m from the shot point are comparable to Chicxulub's (dry: 2.5–4.7 km/s, saturated: 3.2–5.2 km/s). However, for such postexplosion velocities, the measured porosities vary little compared to their intact counterparts, rarely exceeding 4%. Gas permeability measurements performed in situ in the vicinity of shot points (crushed and fractured granites) at both sites are highly variable, between 1 and 10^3 mD. Although the lower part of this range of values compares with the higher permeability measured on Chicxulub granite samples, these in situ measurements do not focus on the same scale and might be subject to the occurrence of macro cracks and fractures that do not occur in the samples presented in this study. No laboratory permeability data set, acquired with increasing P_{eff} on other experimentally shocked granitoid rocks, was found in the literature to compare with Chicxulub sample.

5.3. Previous Assumptions About Porosity, Permeability, and Hydrothermal System

In a model of the postimpact hydrothermal system (Abramov & Kring, 2007), several assumptions about porosity and permeability were made for the lithologies occurring below the crater. Rock porosity was taken to be 25% at the top of the suevite sequence, based on measurements in Yax-1 core (Mayr et al., 2005) and assumed to decay exponentially with depth, z, to account for pore space closing by lithostatic pressure

$$\phi = \phi_0 \, e^{(-z/K)}$$

where K is 1.07 km for Earth (Clifford, 1993, dashed line in Figure 2—porosity column). Site M0077A porosity at the top of the suevite is 31% (Figure 2), a little higher than that assumed previously. The data presented in this study do not fit the modeled exponential decay of porosity with depth, but the recovered material in the core was modified by postimpact processes, including hydrothermal and diagenetic mineralization, compaction, and lithification.

Permeability was also assumed to decrease exponentially with depth (dashed line in Figure 2—permeability column) as pressure increased in the model of the hydrothermal system (Abramov & Kring, 2007), which can be examined anew. After the crater was formed, the peak-ring sampled at site M0077A was submerged by ~600 m of water. The top of the suevite at that depth would have had a pressure of ~6 MPa. The base of the suevite would have had a pressure ~10 MPa, and the bottom of the core would have approached 40 MPa (Kring & Bach, 2021), consistent with the range of effective pressures used to determine permeability above (Section 3.3).

Permeability is also a function of temperature and would have evolved as the hydrothermal system cooled. The model assumed an initial surface permeability of 1 mD at surface temperatures and decreased to 10^{-8} mD at depth or near the impact melt sheet where $T > 500$ °C. In the suevites from Unit 2, measured permeability values range from 0.34 to 2.4 mD. Because permeability likely decreased over time due to compaction and precipitation of hydrothermal clay and other minerals, the initial surface permeability of 1 mD used by Abramov and Kring (2007) seems adequate. It is possible that the exponential decay of that porosity with depth may have been too steep, but this may also depend on the scale of the model as discussed further below.

Initial surface permeabilities of 0.1 and 10 mD were also modeled and shown to affect the thermal evolution of the hydrothermal system and, thus, the duration that hydrothermal fluids affected different parts of the crater. Based on the values measured here, an initial surface permeability of 0.1 mD may be too low, but that—again—may depend on the scale of the model. If the initial surface permeability is 10 mD, then modeled water and steam fluxes are about a factor of 10 higher than that of a 1 mD system. That permeability also creates large upwelling and downwelling plumes that can produce a heterogeneous distribution of sea floor vents. Initial surface permeabilities of 0.1, 1, and 10 mD produce modeled durations of hydrothermal activity of 1.5, 1.7, and 2.3 million years, respectively (Abramov & Kring, 2007), which are collectively a little less than the >2 million years inferred from site M0077A data (Kring et al., 2020). This suggests that other factors, such as potential impediments to fluid flow, should be included in future models. As discussed in Section 5.1, impact melt rocks cutting through peak-ring granitoid rocks may have impeded fluid flow.

It may seem counterintuitive that the lifetime of the hydrothermal system increases as permeability increases (Figure 7 of Abramov and Kring (2007)). That relationship between permeability and system lifetime is, in part, a function of how lifetime is defined. System lifetime was defined as the time to cool below 90 °C within 1 km of the surface, with 90 °C being approximately a doubling of geothermal temperature at that depth. If that temperature or depth was modified, so too would the calculated lifetime.

An increase in system lifetime with increasing permeability is also a consequence of complexities in fluid circulation. In the case of Chicxulub, hydrothermal flow carries heat from depth to the surface, mitigating the cooling effects normally attributed to circulating fluids. The system is effectively a heat pump that is most effective when permeability is high and fluids efficiently carry heat to the surface. In craters of other sizes, multiple vigorous convection cells can be generated. In those cases, system lifetime decreases with increasing permeability (Figure 11 of Abramov and Kring (2005)).

6. Conclusion

The dominant lithology of the recovered section of Chicxulub's peak ring consists of shocked granitoid rocks. Previous studies (Christeson et al., 2018; Morgan et al., 2017; Rae et al., 2019a) pointed at the unique nature of these target rocks, characterized by relatively high porosity. This study is in agreement with previous observations and brings more in-depth data that allow to better understand how the impact event affected the physical properties of the granite:

1. The electrical properties of the granites of Chicxulub's peak ring show that the cementation exponent m (1.59–1.87) is comparable to values typically observed in the lower part of the range of sandstones (1.5–2.5). This suggests that the intense fracturing (as illustrated with ^{14}C-PMMA porosity mapping) of the material makes Chicxulub granite behave more as a cohesive or moderately cemented clastic rock than a microfractured or a microcracked intact granite. The surface conductivity of these granites is close to the surface conductivity of known intact granitoid rocks from the literature. It indicates that if this granite was thermally altered after the impact, altered minerals were partially cleared out

2. The granite recovered from the peak ring has high permeabilities and appears to be relatively insensitive to increasing effective pressure. This insensitivity, associated with pervasive fracturing, as observed in PMMA, and higher V_p despite higher porosity than other cracked granitoid rocks from the literature, suggest that Chicxulub shocked granite does not behave like its peers owing to the high degree of damage. Like with the electrical properties, permeability data points at a behavior closer to a cohesive or moderately cemented clastic rock than to a fractured crystalline rock
3. The results suggest the permeability values used in models of hydrothermal circulation need to be adjusted as a function of depth of the system being explored. Permeabilities of order 0.1 and 10 mD are suitable for portions of the system, including the uppermost suevite unit that covers the Chicxulub peak ring. A permeability of order 0.1 mD, however, may better represent system-wide hydrothermal flow due to local impediments to flow, such as impact melt rock intervals that pervade uplifted granitoid rocks in the Chicxulub peak ring. Models using that lower permeability (Abramov & Kring, 2007) suggest hydrothermal activity persisted for 2.3 million years, which is consistent with values derived from site M0077A petrology and geochemistry (Kring et al., 2020)

Independent petrophysical measurements lead to the same conclusion for the characterization of the granitoid rocks. Other lithologies analyzed in this study include clast-supported suevites (Unit 2) and melt-rich facies (including suevites and impact melt rocks from Units 3 and 4); the latter seems to point at lower permeability than the granites. Observations reported here suggest impact melt rocks cutting through peak-ring granitoid rocks may have acted as a barrier, slowing, or deviating fluid flow. This does not take in account fracture-induced permeability, especially more abundant along lithological contacts within impactites and between impactites and target rocks (Zürcher & Kring, 2004).

Appendix A: Expedition 364 Science Party

S. P. S. Gulick[1], J. V. Morgan[2], T. J. Bralower[3], E. Chenot[4], G. L. Christeson[5], P. Claeys[6], C. S. Cockell[7], M. J. L. Coolen[8], L. Ferrière[9], C. Gebhardt[10], K. Goto[11], S. Green[12], H. Jones[13], D. A. Kring[14], J. Lofi[15], C. M. Lowery[5], R. Ocampo-Torres[16], L. Perez-Cruz[17], A. E. Pickersgill[18], M. H. Poelchau[19], A. S. P. Rae[20], C. Rasmussen[5, 21], M. Rebolledo Vieyra[22], U. Riller[23], H. Sato[24], J. Smit[25], S. M. Tikoo[26], N. Tomioka[27], J. Urrutia-Fucugauchi[17], M. T. Whalen[28], A. Wittmann[29], L. Xiao[30], and K. E. Yamaguchi[31]

[1]Institute for Geophysics and Department of Geological Sciences, Jackson School of Geosciences, University of Texas at Austin, Austin, TX, USA, [2]Department of Earth Science and Engineering, Imperial College London, London, UK, [3]Department of Geosciences, Pennsylvania State University, State College, PA, USA, [4]UniLaSalle, Beauvais, France, [5]Institute for Geophysics, Jackson School of Geosciences, University of Texas at Austin, Austin, TX, USA, [6]Analytical, Environmental and GeoChemistry, Vrije Universiteit Brussel, Brussels, Belgium, [7]Centre for Astrobiology, School of Physics and Astronomy, University of Edinburgh, Edinburgh, UK, [8]Department of Chemistry, WA Organic and Isotope Geochemistry Centre, Curtin University, Perth, Western Australia, Australia, [9]Natural History Museum, Vienna, Austria, [10]Alfred Wegener Institute Helmholtz Centre of Polar and Marine Research, Bremerhaven, Germany, [11]Department of Earth and Planetary Science, University of Tokyo, Japan, [12]British Geological Survey, Edinburgh, UK, [13]Department of Geosciences, Pennsylvania State University, University Park, PA, USA, [14]Lunar and Planetary Institute, Houston, TX, USA, [15]Géosciences Montpellier, Université de Montpellier, Montpellier, France, [16]Groupe de Physico Chimie de l'Atmosphère, L'Institut de Chimie et Procédés pour l'Ènergie, l'Environnement et la Santé (ICPEES), Université de Strasbourg, Strasbourg, France, [17]Instituto de Geofísica, Universidad Nacional Autónoma De México, Mexico, Mexico, [18]School of Geographical and Earth Sciences, University of Glasgow, Glasgow, Now at: Argon Isotope Facility, Scottish Universities Environmental Research Centre, East Kilbride, UK, [19]Institut für Geound Umweltnaturwissenschaften, Albert Ludwigs Universität, Freiburg, Germany, [20]Department of Earth Science, University of Cambridge, Cambridge, UK, [21]Department of Geology and Geophysics, University of Utah, Salt Lake City, UT, USA, [22]Independent consultant, Cancun, Mexico, [23]Institut für Geologie, Universität Hamburg, Hamburg, Germany, [24]Japan Agency for Marine Earth Science and Technology, Kanagawa, Japan, [25]Faculty of Earth and Life Sciences (FALW), Vrije Universiteit Amsterdam, Amsterdam, Netherlands, [26]Department of Geophysics, Stanford University, Stanford, California USA, [27]Kochi Institute for Core Sample Research, Japan Agency for Marine Earth Science and Technology, Kochi, Japan, [28]Department of Geosciences, University of Alaska Fairbanks, Fairbanks,

AK, USA, [29]Eyring Materials Center, Arizona State University, Tempe, AZ, USA, [30]School of Earth Sciences, Planetary Science Institute, China University of Geosciences, Wuhan, China, [31]Department of Chemistry, Toho University, and NASA Astrobiology Institute.

Data Availability Statement

Data produced for this study are presented in Table 1, including their IGSN, and are available here: DOI 10.5281/zenodo.6426690. Data used for comparisons in this study can be found in the references listed in Table 2. Figures 2, 3, 5, and 6 were designed with Python (http://www.python.org, v3.7), using Pandas (McKinney, 2010, v1.2), Numpy (Harris et al., 2020, v1.19), and Matplotlib (Hunter, 2007, v3.4).

Acknowledgments
The authors thank the International Ocean Discovery Program. This study uses shipboard samples from the Expedition 364 *Chicxulub: drilling the K-Pg Impact Crater* implemented under the International Ocean Discovery Program (IODP) and the International Continental Scientific Drilling Project (ICDP) by the European Consortium for Ocean Research Drilling (ECORD). LPI Contribution No. 2673. The authors thank the reviewers for their corrections and useful suggested references.

References

Abramov, O., & Kring, D. A. (2004). Numerical modeling of an impact-induced hydrothermal system at the Sudbury crater. *Journal of Geophysical Research*, *109*, E10007. https://doi.org/10.1029/2003JE002213

Abramov, O., & Kring, D. A. (2005). Impact-induced hydrothermal activity on early Mars. *Journal of Geophysical Research*, *110*, E12S09. https://doi.org/10.1029/2005JE002453

Abramov, O., & Kring, D. A. (2007). Numerical modeling of impact-induced hydrothermal activity at the Chicxulub crater. *Meteoritics & Planetary Science*, *42*(1), 93–112. https://doi.org/10.1111/j.1945-5100.2007.tb00220.x

Archie, G. E. (1942). The electrical resistivity log as an aid in determining some reservoir characteristics. *Transactions of the AIME*, *146*(1), 54–62. https://doi.org/10.2118/942054-G

Belghoul, A. (2007). *Caractérisation pétrophysique et hydrodynamique du socle cristallin. Géophysique [physics.geo-ph]. Université Montpellier II-Sciences et Techniques du Languedoc*. Retrieved from https://tel.archives-ouvertes.fr/tel-00444175

Benson, P. M., Meredith, P. G., & Schubnel, A. (2006). Role of void space geometry in permeability evolution in crustal rocks at elevated pressure. *Journal of Geophysical Research*, *111*, B12203. https://doi.org/10.1029/2006JB004309

Bernabe, Y. (1988). Comparison of the effective pressure law for permeability and resistivity formation factor in Chelmsford granite. *Pure and Applied Geophysics*, *127*(4), 607–625. https://doi.org/10.1007/BF00881747

Bernard, M.-L., Zamora, M., Géraud, Y., & Boudon, G. (2007). Transport properties of pyroclastic rocks from Montagne Pelée volcano (Martinique, lesser Antilles). *Journal of Geophysical Research*, *112*, B05205. https://doi.org/10.1029/2006JB004385

Boardman, C. R., & Skrove, J. (1966). Distribution in fracture permeability of a granitic rock mass following a contained nuclear explosion. *Journal of Petroleum Technology*, *18*, 619–623. https://doi.org/10.2118/1358-PA

Brace, W. F. (1977). Permeability from resistivity and pore shape. *Journal of Geophysical Research*, *82*(23), 3343–3349. https://doi.org/10.1029/JB082i023p03343

Brace, W. F. (1980). Permeability of crystalline and argillaceous rocks. *International Journal of Rock Mechanics and Mining Sciences & Geomechanics Abstracts*, *17*(5), 241–251. https://doi.org/10.1016/0148-9062(80)90807-4

Brace, W. F., Walsh, J. B., & Frangos, W. T. (1968). Permeability of granite under high pressure. *Journal of Geophysical Research*, *73*(6), 2225–2236. https://doi.org/10.1029/JB073i006p02225

Cassiaux, M. (2004). *Pétrographie et pétrophysique des matrices granitiques: relation entre porosité et propriétés de transport*. Poitiers.

Christeson, G. L., Gulick, S. P. S., Morgan, J. V., Gebhardt, C., Kring, D. A., Le Ber, E., et al. (2018). Extraordinary rocks from the peak ring of the Chicxulub Impact Crater: P-wave velocity, density, and porosity measurements from IODP/ICDP Expedition 364. *Earth and Planetary Science Letters*, *495*, 1–11. https://doi.org/10.1016/j.epsl.2018.05.013

Christeson, G. L., Morgan, J. V., & Gulick, S. P. S. (2021). Mapping the Chicxulub impact stratigraphy and peak ring using drilling and seismic data. *Journal of Geophysical Research: Planets*, *126*, e2021JE006938. https://doi.org/10.1029/2021JE006938

Clifford, S. M. (1993). A model for the hydrologic and climatic behavior of water on Mars. *Journal of Geophysical Research*, *98*(E6), 10973. https://doi.org/10.1029/93JE00225

Cockell, C. S. (2006). The origin and emergence of life under impact bombardment. *Philosophical Transactions of the Royal Society B: Biological Sciences*, *361*(1474), 1845–1856. https://doi.org/10.1098/rstb.2006.1908

David, C., Menéndez, B., & Darot, M. (1999). Influence of stress-induced and thermal cracking on physical properties and microstructure of La Peyratte granite. *International Journal of Rock Mechanics and Mining Sciences*, *36*(4), 433–448. https://doi.org/10.1016/S0148-9062(99)00010-8

David, C., Wassermann, J., Amann, F., Lockner, D. A., Rutter, E. H., Vanorio, T., et al. (2018). KG^{2}B, a collaborative benchmarking exercise for estimating the permeability of the Grimsel granodiorite—Part 1: Measurements, pressure dependence and pore-fluid effects. *Geophysical Journal International*, *215*(2), 799–824. https://doi.org/10.1093/gji/ggy304

David, C., Wong, T.-F., Zhu, W., & Zhang, J. (1994). Laboratory measurement of compaction-induced permeability change in porous rocks: Implications for the generation and maintenance of pore pressure excess in the crust. *Pure and Applied Geophysics*, *143*(1–3), 425–456. https://doi.org/10.1007/BF00874337

de Graaff, S. J., Kaskes, P., Déhais, T., Goderis, S., Vinciane, D., Ross, C. H., et al. (2021). *New insights into the formation and emplacement of impact melt rocks within the Chicxulub impact structure, following the 2016 IODP-ICDP Expedition 364*. Geological Society of America Bulletin. https://doi.org/10.1130/B35795.1

Derlich, S. (1970a). *Explosions nucléaires souterraines—étude des zones de fractures*. *Rapport CEA-R-3941*.

Derlich, S. (1970b). Underground nuclear explosion effects in granite rock fracturing. In *Symposium on Engineering with Nuclear Explosives* (Vol. 1, pp. 14).

Elbra, T., & Pesonen, L. J. (2011). Physical properties of the Yaxcopoil-1 deep drill core, Chicxulub impact structure, Mexico. *Meteoritics & Planetary Science*, *46*(11), 1640–1652. https://doi.org/10.1111/j.1945-5100.2011.01253.x

Fortin, J., Stanchits, S., Vinciguerra, S., & Guéguen, Y. (2011). Influence of thermal and mechanical cracks on permeability and elastic wave velocities in a basalt from Mt. Etna volcano subjected to elevated pressure. *Tectonophysics*, *503*(1–2), 60–74. https://doi.org/10.1016/j.tecto.2010.09.028

Géraud, Y., Rosener, M., Surma, F., Place, J., Le Garzic, É., & Diraison, M. (2010). Physical properties of fault zones within a granite body: Example of the Soultz-sous-Forêts geothermal site. *Comptes Rendus Geoscience*, *342*(7–8), 566–574. https://doi.org/10.1016/j.crte.2010.02.002

Ghorbani, A., Revil, A., Coperey, A., Soueid Ahmed, A., Roque, S., Heap, M. J., et al. (2018). Complex conductivity of volcanic rocks and the geophysical mapping of alteration in volcanoes. *Journal of Volcanology and Geothermal Research*, *357*, 106–127. https://doi.org/10.1016/j.jvolgeores.2018.04.014

Glover, P. W. J., Gómez, J. B., Meredith, P. G., Hayashi, K., Sammonds, P. R., & Murrell, S. A. F. (1997). Damage of saturated rocks undergoing triaxial deformation using complex electrical conductivity measurements: Experimental results. *Physics and Chemistry of the Earth*, *22*(1–2), 57–61. https://doi.org/10.1016/S0079-1946(97)00078-5

Gulick, S. P. S., Bralower, T. J., Ormö, J., Hall, B., Grice, K., Schaefer, B., et al. (2019). The first day of the Cenozoic. *Proceedings of the National Academy of Sciences of the United States of America*, *116*(39), 19342–19351. https://doi.org/10.1073/pnas.1909479116

Gulick, S. P. S., Morgan, J. V., Mellett, C. L., & Urrutia-Fucugauchi, J. (2016). Expedition 364 Scientific prospectus: Chicxulub: Drilling the K-Pg impact crater: International Ocean Discovery Program. https://doi.org/10.14379/iodp.sp.364.2016

Harris, C. R., Millman, K. J., van der Walt, S. J., Gommers, R., Virtanen, P., Cournapeau, D., et al. (2020). Array programming with NumPy. *Nature*, *585*(7825), 357–362. https://doi.org/10.1038/s41586-020-2649-2

Heap, M. J., Reuschlé, T., Farquharson, J. I., & Baud, P. (2018). Permeability of volcanic rocks to gas and water. *Journal of Volcanology and Geothermal Research*, *354*, 29–38. https://doi.org/10.1016/j.jvolgeores.2018.02.002

Hellmuth, K. H., Siitari-Kauppi, M., & Lindberg, A. (1993). Study of porosity and migration pathways in crystalline rock by impregnation with ^{14}C-polymethylmethacrylate. *Journal of Contaminant Hydrology*, *13*(1–4), 403–418. https://doi.org/10.1016/0169-7722(93)90073-2

Hunter, J. D. (2007). Matplotlib: A 2D graphics environment. *Computing in Science & Engineering*, *9*(3), 90–95. https://doi.org/10.1109/MCSE.2007.55

Ildefonse, B., & Pezard, P. A. (2001). Electrical properties of slow-spreading ridge gabbros from ODP Site 735, Southwest Indian Ridge. *Tectonophysics*, *330*(1–2), 69–92. https://doi.org/10.1016/S0040-1951(00)00220-1

Kaskes, P., de Graaff, S. J., Feignon, J. G., Déhais, T., Goderis, S., Ferrière, L., et al. (2021). Formation of the crater suevite sequence from the Chicxulub peak ring: A petrographic, geochemical, and sedimentological characterization. *Geological Society of America Bulletin*, *134*(3–4), 895–927. https://doi.org/10.1130/B36020.1

Kelokaski, M., Siitari-Kauppi, M., Sardini, P., Möri, A., & Hellmuth, K. H. (2006). Characterisation of pore space geometry by ^{14}C-PMMA impregnation—Development work for in situ studies. *Journal of Geochemical Exploration*, *90*(1–2), 45–52. https://doi.org/10.1016/j.gexplo.2005.09.005

Kennedy, B. M., Farquhar, A., Hilderman, R., Villeneuve, M. C., Heap, M. J., Mordensky, S., et al. (2020). Pressure controlled permeability in a conduit filled with fractured hydrothermal breccia reconstructed from Ballistics from Whakaari (White Island), New Zealand. *Geosciences*, *10*(4), 138. https://doi.org/10.3390/geosciences10040138

Klinkenberg, L. J. (1941). The permeability of porous media to liquids and gases. *Drilling and Production Practice*, 200–213. https://doi.org/10.5510/OGP20120200114

Kranz, R. L., Frankel, A. D., Engelder, T., & Scholz, C. H. (1979). The permeability of whole and jointed Barre Granite. *International Journal of Rock Mechanics and Mining Sciences & Geomechanics Abstracts*, *16*(4), 225–234. https://doi.org/10.1016/0148-9062(79)91197-5

Kring, D. A. (2000). Impact events and their effect on the origin, evolution, and distribution of life. *Geological Society of America Today*, *10*(8), 1–7.

Kring, D. A., & Bach, W. (2021). Hydrogen production from alteration of Chicxulub crater impact breccias: Potential energy source for a subsurface microbial ecosystem. *Astrobiology*, *21*(12), 1547–1564. https://doi.org/10.1089/ast.2021.0045

Kring, D. A., & Boynton, W. V. (1992). Petrogenesis of an augite-bearing melt rock in the Chicxulub structure and its relationship to K/T impact spherules in Haiti. *Nature*, *358*(6382), 141–144. https://doi.org/10.1038/358141a0

Kring, D. A., Claeys, P., Riller, U., Xiao, L., Collins, G. S., Ferrière, L., et al. (2017). Emplacing impact melt in the Chicxulub peak ring. In *Lunar and Planetary Science XLVIII*. Retrieved from https://www.hou.usra.edu/meetings/lpsc2017/pdf/1213.pdf

Kring, D. A., Hörz, F., Zurcher, L., & Fucugauchi, J. U. (2004). Impact lithologies and their emplacement in the Chicxulub impact crater: Initial results from the Chicxulub Scientific Drilling Project, Yaxcopoil, Mexico. *Meteoritics & Planetary Science*, *39*(6), 879–897. https://doi.org/10.1111/j.1945-5100.2004.tb00936.x

Kring, D. A., Tikoo, S. M., Schmieder, M., Riller, U., Rebolledo-Vieyra, M., Simpson, S. L., et al. (2020). Probing the hydrothermal system of the Chicxulub impact crater. *Science Advances*, *6*(22), eaaz3053. https://doi.org/10.1126/sciadv.aaz3053

Kring, D. A., Whitehouse, M. J., & Schmieder, M. (2021). Microbial sulfur isotope fractionation in the Chicxulub hydrothermal system. *Astrobiology*, *21*(1), 103–114. https://doi.org/10.1089/ast.2020.2286

Lockner, D. A., Tanaka, H., Ito, H., Ikeda, R., Omura, K., & Naka, H. (2009). Geometry of the Nojima fault at Nojima-Hirabayashi, Japan—I. A simple damage structure inferred from borehole core permeability. *Pure and Applied Geophysics*, *166*(10–11), 1649–1667. https://doi.org/10.1007/s00024-009-0515-0

Mayr, S., Burkhardt, H., Popov, Y., Romushkevich, R., & Bayuk, I. (2005). Geothermal and petrophysical investigations within the Chicxulub Scientific Drilling Project—Physical properties of rocks in the borehole Yax-1. In *Integrated Ocean Drilling Program/International Continental Drilling Program Joint Meeting*.

Mayr, S., Burkhardt, H., Popov, Y., & Wittmann, A. (2008a). Estimation of hydraulic permeability considering the micro morphology of rocks of the borehole YAXCOPOIL-1 (Impact crater Chicxulub, Mexico). *International Journal of Earth Sciences*, *97*(2), 385–399. https://doi.org/10.1007/s00531-007-0227-6

Mayr, S., Wittmann, A., Burkhardt, H., Popov, Y., Romushkevich, R., Bayuk, I., et al. (2008b). Integrated interpretation of physical properties of rocks of the borehole Yaxcopoil-1 (Chicxulub impact structure). *Journal of Geophysical Research*, *113*, B07201. https://doi.org/10.1029/2007JB005420

McCall, N., Gulick, S. P. S., Hall, B., Rae, A. S. P., Poelchau, M. H., Riller, U., et al. (2021). Orientations of planar cataclasite zones in the Chicxulub peak ring as a ground truth for peak ring formation models. *Earth and Planetary Science Letters*, *576*, 117236. https://doi.org/10.1016/j.epsl.2021.117236

McCarville, P., & Crossey, L. J. (1996). Post-impact hydrothermal alteration of the Manson impact structure. In *Special Paper 302 the Manson impact structure Iowa anatomy of an impact crater*. Geological Society of America. https://doi.org/10.1130/0-8137-2302-7.347

McKinney, W. (2010). *Data structures for statistical computing in Python* (pp. 56–61). https://doi.org/10.25080/Majora-92bf1922-00a

Mizoguchi, K., Hirose, T., Shimamoto, T., & Fukuyama, E. (2008). Internal structure and permeability of the Nojima fault, southwest Japan. *Journal of Structural Geology*, *30*(4), 513–524. https://doi.org/10.1016/j.jsg.2007.12.002

Moore, D. E., Lockner, D. A., Ito, H., Ikeda, R., Tanaka, H., & Omura, K. (2009). Geometry of the Nojima fault at Nojima-Hirabayashi, Japan—II. Microstructures and their implications for permeability and strength. *Pure and Applied Geophysics*, *166*(10–11), 1669–1691. https://doi.org/10.1007/s00024-009-0513-2

Morgan, J. V., Gulick, S. P. S., Bralower, T. J., Chenot, E., Christeson, G. L., Claeys, P., et al. (2016). The formation of peak rings in large impact craters. *Science*, *354*(6314), 878–882. https://doi.org/10.1126/science.aah6561

Morgan, J. V., Gulick, S. P. S., Mellett, C. L., Green, S. L., & The Expedition 364 Scientists. (2017). *Chicxulub: Drilling the K-Pg impact crater* (Vol. 364). International Ocean Discovery Program. https://doi.org/10.14379/iodp.proc.364.2017

Morrow, C. A., & Lockner, D. A. (1994). Permeability differences between surface-derived and deep drillhole core samples. *Geophysical Research Letters*, *21*(19), 2151–2154. https://doi.org/10.1029/94GL01936

Morrow, C. A., & Lockner, D. A. (1997). Permeability and porosity of the Illinois UPH 3 drillhole granite and a comparison with other deep drillhole rocks. *Journal of Geophysical Research*, *102*(B2), 3067–3075. https://doi.org/10.1029/96JB03178

Nara, Y., Meredith, P. G., Yoneda, T., & Kaneko, K. (2011). Influence of macro-fractures and micro-fractures on permeability and elastic wave velocities in basalt at elevated pressure. *Tectonophysics*, *503*(1–2), 52–59. https://doi.org/10.1016/j.tecto.2010.09.027

Nasseri, M. H. B., Schubnel, A., Benson, P. M., & Young, R. P. (2009). Common evolution of mechanical and transport properties in thermally cracked westerly granite at elevated hydrostatic pressure. *Pure and Applied Geophysics*, *166*(5–7), 927–948. https://doi.org/10.1007/s00024-009-0485-2

Nasseri, M. H. B., Schubnel, A., & Young, R. P. (2007). Coupled evolutions of fracture toughness and elastic wave velocities at high crack density in thermally treated Westerly granite. *International Journal of Rock Mechanics and Mining Sciences*, *44*(4), 601–616. https://doi.org/10.1016/j.ijrmms.2006.09.008

Naumov, M. V. (1996). Basic regularities of the postimpact hydrothermal process. *Solar System Research*, *30*(1), 21.

Nur, A., & Simmons, G. (1969). The effect of saturation on velocity in low porosity rocks. *Earth and Planetary Science Letters*, *7*(2), 183–193. https://doi.org/10.1016/0012-821X(69)90035-1

Oila, E., Sardini, P., Siitari-Kauppi, M., & Hellmuth, K. H. (2005). The ^{14}C-polymethylmethacrylate (PMMA) impregnation method and image analysis as a tool for porosity characterization of rock-forming minerals. *Geological Society of London, Special Publications*, *240*(1), 335–342. https://doi.org/10.1144/gsl.sp.2005.240.01.24

Osinski, G. R., Spray, J. G., & Lee, P. (2001). Impact-induced hydrothermal activity within the Haughton impact structure, arctic Canada: Generation of a transient, warm, wet oasis. *Meteoritics & Planetary Science*, *36*(5), 731–745. https://doi.org/10.1111/j.1945-5100.2001.tb01910.x

Owens, W. (1979). *Geoscience parameter data base handbook: Granites and basalts*. Livermore, CA. https://doi.org/10.2172/5719576

Pérez-Flores, P., Wang, G., Mitchell, T. M., Meredith, P. G., Nara, Y., Sarkar, V., & Cembrano, J. (2017). The effect of offset on fracture permeability of rocks from the Southern Andes Volcanic Zone, Chile. *Journal of Structural Geology*, *104*, 142–158. https://doi.org/10.1016/j.jsg.2017.09.015

Pezard, P. A., Hermitte, D., Revil, A., Virlogueux, D., Leutsch, Y., & Harvey, P. K. (1999a). Physical properties of granite, with application to nuclear waste storage in the subsurface. In *Texture and physical properties of rocks* (pp. 149–151).

Pezard, P. A., Ito, H., Hermitte, D., & Revil, A. (1999b). Electrical properties and alteration of granitodiorites from the GSJ Hirabayashi hole, Japan. In *Proceedings of the International Workshop on the Nojima Fault Core and Borehole Data Analysis* (pp. 255–262).

Popov, Y., Mayr, S., Romushkevich, R., Burkhardt, H., & Wilhelm, H. (2014). Comparison of petrophysical properties of impactites for four meteoritic impact structures. *Meteoritics & Planetary Science*, *49*(5), 896–920. doi https://doi.org/10.1111/maps.12299

Popov, Y., Pohl, J., Romushkevich, R., Tertychnyi, V., & Soffel, H. (2003). Geothermal characteristics of the Ries impact structure. *Geophysical Journal International*, *154*(2), 355–378. https://doi.org/10.1046/j.1365-246X.2003.01925.x

Rae, A. S. P., Collins, G. S., Morgan, J. V., Salge, T., Christeson, G. L., Leung, J., et al. (2019a). Impact-induced porosity and microfracturing at the Chicxulub impact structure. *Journal of Geophysical Research: Planets*, *124*, 1960–1978. doi https://doi.org/10.1029/2019JE005929

Rae, A. S. P., Collins, G. S., Poelchau, M., Riller, U., Davison, T. M., Grieve, R. A. F., et al. (2019b). Stress-strain evolution during peak-ring formation: A case study of the Chicxulub impact structure. *Journal of Geophysical Research: Planets*, *124*, 396–417. https://doi.org/10.1029/2018JE005821

Rathbun, J. A., & Squyres, S. W. (2002). Hydrothermal systems associated with Martian impact craters. *Icarus*, *157*(2), 362–372. https://doi.org/10.1006/icar.2002.6838

Revil, A., & Cathles, L. M. (1999). Permeability of shaly sands. *Water Resources Research*, *35*(3), 651–662. https://doi.org/10.1029/98WR02700

Revil, A., Kessouri, P., & Torres-Verdín, C. (2014). Electrical conductivity, induced polarization, and permeability of the Fontainebleau sandstone. *Geophysics*, *79*(5), D301–D318. https://doi.org/10.1190/geo2014-0036.1

Revil, A., Qi, Y., Ghorbani, A., Coperey, A., Ahmed, A. S., Finizola, A., & Ricci, T. (2019). Induced polarization of volcanic rocks. 3. Imaging clay cap properties in geothermal fields. *Geophysical Journal International*, *218*(2), 1398–1427. https://doi.org/10.1093/gji/ggz207

Riller, U., Poelchau, M., Rae, A. S. P., Schulte, F. M., Collins, G. S., Melosh, H. J., et al. (2018). Rock fluidization during peak-ring formation of large impact structures. *Nature*, *562*(7728), 511–518. https://doi.org/10.1038/s41586-018-0607-z

Rosener, M. (2007). *Etude pétrophysique et modélisation des effets des transferts thermiques entre roche et fluide dans le contexte géothermique de Soultz-sous-Forêts. Université Louis Pasteur—Strasbourg I*. Retrieved from https://tel.archives-ouvertes.fr/tel-00202959

Sardini, P., Caner, L., Mossler, P., Mazurier, A., Hellmuth, K. H., Graham, R. C., et al. (2015). Calibration of digital autoradiograph technique for quantifying rock porosity using ^{14}C-PMMA method. *Journal of Radioanalytical and Nuclear Chemistry*, *303*(1), 11–23. https://doi.org/10.1007/s10967-014-3617-9

Sardini, P., El Albani, A., Pret, D., Gaboreau, S., Siitari-Kauppi, M., & Beaufort, D. (2009). Mapping and quantifying the clay aggregate microporosity in medium- to coarse-grained sandstones using the ^{14}C-PMMA method. *Journal of Sedimentary Research*, *79*, 584–592. https://doi.org/10.2110/jsr.2009.063

Sardini, P., Robinet, J. C., Siitari-Kauppi, M., Delay, F., & Hellmuth, K. H. (2007). Direct simulation of heterogeneous diffusion and inversion procedure applied to an out-diffusion experiment. Test case of Palmottu granite. *Journal of Contaminant Hydrology*, *93*(1–4), 21–37. https://doi.org/10.1016/j.jconhyd.2007.01.011

Sardini, P., Siitari-Kauppi, M., Beaufort, D., & Hellmuth, K. H. (2006). On the connected porosity of mineral aggregates in crystalline rocks. *American Mineralogist*, *91*(7), 1069–1080. https://doi.org/10.2138/am.2006.1939

Sarout, J., Cazes, E., Delle Piane, C., Arena, A., & Esteban, L. (2017). Stress-dependent permeability and wave dispersion in tight cracked rocks: Experimental validation of simple effective medium models. *Journal of Geophysical Research: Solid Earth*, *122*, 6180–6201. https://doi.org/10.1002/2017JB014147

Schild, M., Siegesmund, S., Vollbrecht, A., & Mazurek, M. (2001). Characterization of granite matrix porosity and pore-space geometry by in situ and laboratory methods. *Geophysical Journal International*, *146*(1), 111–125. https://doi.org/10.1046/j.0956-540x.2001.01427.x

Schön, J. (2015). *Physical properties of rocks: Fundamentals and principles of petrophysics*. Elsevier.

Schulte, F. M., Wittmann, A., Jung, S., Morgan, J. V., Gulick, S. P. S., Kring, D. A., et al. (2021). Ocean resurge-induced impact melt dynamics on the peak-ring of the Chicxulub impact structure, Mexico. *International Journal of Earth Sciences*, *110*(7), 2619–2636. https://doi.org/10.1007/s00531-021-02008-w

Short, N. M. (1966). Effects of shock pressures from a nuclear explosion on mechanical and optical properties of granodiorite. *Journal of Geophysical Research*, *71*(4), 1195–1215. https://doi.org/10.1029/JZ071i004p01195

Siitari-Kauppi, M. (2002). *Development of ^{14}C-polymethylmethacrylate method for the characterisation of low porosity media. Application to rocks in geological barriers of nuclear waste storage*. Helsinki and Poitiers.

Simpson, S. L., Osinski, G. R., Longstaffe, F. J., Schmieder, M., & Kring, D. A. (2020). Hydrothermal alteration associated with the Chicxulub impact crater upper peak-ring breccias. *Earth and Planetary Science Letters*, *547*, 116425. https://doi.org/10.1016/j.epsl.2020.116425

Soueid Ahmed, A., Revil, A., Byrdina, S., Coperey, A., Gailler, L., Grobbe, N., et al. (2018). 3D electrical conductivity tomography of volcanoes. *Journal of Volcanology and Geothermal Research*, *356*, 243–263. https://doi.org/10.1016/j.jvolgeores.2018.03.017

Stöffler, D., & Grieve, R. (2007). Impactites. In J. Fettes, D., & Desmons (Ed.), *Metamorphic rocks: A classification and glossary of terms, recommendations of the international union of geological sciences* (pp. 82–125).

Sueyoshi, K., Yokoyama, T., & Katayama, I. (2020). Experimental measurement of the transport flow path aperture in thermally cracked granite and the relationship between pore structure and permeability. *Geofluids*, *2020*, 1–10. https://doi.org/10.1155/2020/8818293

Tanikawa, W., & Shimamoto, T. (2009). Comparison of Klinkenberg-corrected gas permeability and water permeability in sedimentary rocks. *International Journal of Rock Mechanics and Mining Sciences*, *46*(2), 229–238. https://doi.org/10.1016/j.ijrmms.2008.03.004

Timms, N. E., Kirkland, C. L., Cavosie, A. J., Rae, A. S. P., Rickard, W. D. A., Evans, N. J., et al. (2020). Shocked titanite records Chicxulub hydrothermal alteration and impact age. *Geochimica et Cosmochimica Acta*, *281*, 12–30. https://doi.org/10.1016/j.gca.2020.04.031

Voutilainen, M., Miettinen, A., Sardini, P., Parkkonen, J., Sammaljärvi, J., Gylling, B., et al. (2019). Characterization of spatial porosity and mineral distribution of crystalline rock using X-ray micro computed tomography, C-14-PMMA autoradiography and scanning electron microscopy. *Applied Geochemistry*, *101*, 50–61. https://doi.org/10.1016/j.apgeochem.2018.12.024

Walsh, J. B., & Brace, W. F. (1984). The effect of pressure on porosity and the transport properties of rock. *Journal of Geophysical Research*, *89*(B11), 9425. https://doi.org/10.1029/JB089iB11p09425

Waxman, M. H., & Smits, L. J. M. (1968). Electrical conductivities in oil-bearing shaly sands. *Society of Petroleum Engineers Journal*, *8*(2), 107–122. https://doi.org/10.2118/1863-A

Wittmann, A., Kenkmann, T., Hecht, L., & Stoffler, D. (2007). Reconstruction of the Chicxulub ejecta plume from its deposits in drill core Yaxcopoil-1. *Geological Society of America Bulletin*, *119*(9–10), 1151–1167. https://doi.org/10.1130/B26116.1

Wyble, D. O. (1958). Effect of applied pressure on the conductivity, porosity and permeability of sandstones. *Journal of Petroleum Technology*, *10*(11), 57–59. https://doi.org/10.2118/1081-G

Yang, S.-Q., Ranjith, P. G., Jing, H.-W., Tian, W.-L., & Ju, Y. (2017). An experimental investigation on thermal damage and failure mechanical behavior of granite after exposure to different high temperature treatments. *Geothermics*, *65*, 180–197. https://doi.org/10.1016/j.geothermics.2016.09.008

Zhang, F., Zhao, J., Hu, D., Skoczylas, F., & Shao, J. (2018). Laboratory investigation on physical and mechanical properties of granite after heating and water-cooling treatment. *Rock Mechanics and Rock Engineering*, *51*(3), 677–694. https://doi.org/10.1007/s00603-017-1350-8

Zhu, W., & Wong, T. (1997). The transition from brittle faulting to cataclastic flow: Permeability evolution. *Journal of Geophysical Research*, *102*(B2), 3027–3041. https://doi.org/10.1029/96JB03282

Zürcher, L., & Kring, D. A. (2004). Hydrothermal alteration in the core of the Yaxcopoil-1 borehole, Chicxulub impact structure, Mexico. *Meteoritics & Planetary Science*, *39*(7), 1199–1221. https://doi.org/10.1111/j.1945-5100.2004.tb01137.x